Journal of Power Sources 666 (2026) 239124

Contents lists available at ScienceDirect

Journal of Power Sources

journal homepage: www.elsevier.com/locate/jpowsour

Highly-cyclable Na-ion battery exploiting a nanostructured tin-carbon anode, layered-oxide P3/P2 cathode and a glyme-based electrolyte

Edoardo Barcaro [a], Daniel Amato [a], Vittorio Marangon [b,c], Dominic Bresser [b,c,d], Jusef Hassoun [a,e,*]

[a] University of Ferrara, Department of Chemical, Pharmaceutical and Agricultural Sciences, Via Fossato di Mortara 17, 44121, Ferrara, Italy
[b] Helmholtz Institute Ulm (HIU), Helmholtzstrasse 11, Ulm, 89081, Germany
[c] Karlsruhe Institute of Technology (KIT), P.O. Box 3640, Karlsruhe, 76021, Germany
[d] Ulm University (UUlm), 89069, Ulm, Germany
[e] CNI@NEST, Istituto Italiano di Tecnologia, P.zza S. Silvestro 12, 56127, Pisa, Italy

HIGHLIGHTS

- Full Na-ion battery combining a P3/P2 layered-oxide cathode and a tin-carbon anode.
- The alloying anode is achieved using CMC binder and water as the casting solvent.
- The full-cell is enabled by chemical sodiation of the alloying-anode.
- The external sodiation allows cell balancing and stabilizes the anode without further treatment.
- The full-cell delivers up to 310 Wh kg^{-1} (cathode) and 175 Wh kg^{-1} (anode & cathode).

GRAPHICAL ABSTRACT

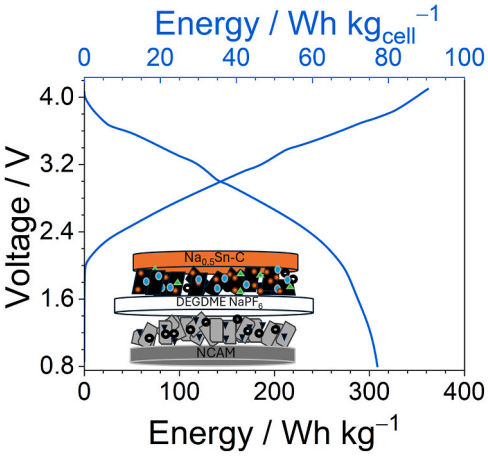

ARTICLE INFO

Keywords:
Sodium-ion battery
Layered-oxide cathode
Tin-carbon anode
Binder
Chemical sodiation
Glyme electrolyte

ABSTRACT

Alternative materials to (purely) carbon-based anodes could enhance the energy density of sodium-ion batteries, and thus favor their complementarity to lithium-ion batteries. This work provides a viable setup of Na-ion cells combining a P3/P2 sodium-deficient layered cathode and a tin-carbon Na-alloying anode with a glyme-based electrolyte. Galvanostatic cycling in sodium half-cells of the water-processed alloying anode with sodium carboxymethyl cellulose (CMC) binder shows a maximum capacity of ~260 mAh g^{-1}, a capacity retention exceeding 70 % after 150 cycles, and an average Coulombic efficiency over 99 %. The multi-metal cathode evidences a great cycling stability over 100 cycles, with average Coulombic efficiency between 99.5 and 99.6 % as favored by the presence of Al^{3+} ions in its structure. Full Na-ion batteries exploiting *ad hoc* chemically-sodiated tin-based anode and sodium-deficient layered cathode operate with average working voltage of 3 V, and maximum

* Corresponding author. University of Ferrara, Department of Chemical, Pharmaceutical and Agricultural Sciences, Via Fossato di Mortara 17, 44121, Ferrara, Italy.
E-mail address: jusef.hassoun@unife.it (J. Hassoun).

https://doi.org/10.1016/j.jpowsour.2025.239124
Received 11 September 2025; Received in revised form 11 November 2025; Accepted 13 December 2025
Available online 26 December 2025

capacity of 120 mAh g^{-1} retained for 95 % over 100 cycles in the best experimental setup. The rationally designed full-cell reaches theoretical energy density between 310 and 250 Wh kg^{-1} as referred to the cathode weight.

1. Introduction

1.1. Sodium-ion batteries

Sodium-ion batteries (SIBs) are attracting massive attention as a possible complementary system to lithium-ion batteries (LIBs), due to the abundant natural reserves of sodium and to the similar electrochemistry based on the rocking-chair mechanism [1]. SIBs are continuously subjected to technical analysis to assess their practical feasibility, which is heavily influenced by price fluctuation due to supply chain variation, thus requesting a detailed techno-economical assessments to keep track of this blooming drop-in technology [2–7]. At the present state, the lower gravimetric and volumetric energy density of SIBs represents the main limiting factor to be addressed in order to match the LIBs performance, by novel and more competing cell designs [8,9]. Besides, pursuing a satisfactory tradeoff between electrochemical performance and overall materials cost is greatly influenced by the choice of the cathode chemistry [10,11], as well as by the adopted electrolyte [12–16]. Furthermore, a potential step forward may be the implementation of alternative anodes, beyond those based on Na-insertion into low-density hard carbons (HCs) and Na-(co)intercalation into graphite [17–20].

1.2. Na-alloying anodes

Na-alloying anodes rely on metallic or non-metallic elements, such as tin (Sn) [21], lead (Pb) [22,23], phosphorus (P) [24–26], or antimony (Sb) [27,28], which can reversibly form alloys with sodium and deliver relevant capacities. Differently from LIBs, the use of silicon (Si) in Na-cells is hindered by the low stability of the corresponding Na-Si alloys, although a recent study shed light on the role of Si as structural stabilizer and redox-active element in multicomponent alloys for SIBs [29]. In general, the alloying process occurs through the multi-step formation of sodiated compounds, which is, however, a kinetically limited reaction, the reversibility of which may be limited by a notable shape variation of the alloying particles depending on the test conditions [30–33]. Despite the concerns risen by the above volumetric expansion upon sodiation [34], Sn, Pb, and P can theoretically offer an attractive volumetric capacity above 1.0 Ah cm^{-3} at the fully sodiated state, which is an essentially two-fold increase with respect to HCs, usually delivering between 0.4 and 0.5 Ah cm^{-3} [35]. In particular, Sn has been suggested as a non-toxic and abundant element with a relevant theoretical capacity of 847 mAh g^{-1}, corresponding to the formation of the fully-sodiated $Na_{15}Sn_4$ alloy [31,33,36]. However, the formation of the above alloys can undermine the mechanical stability and pulverize the electrode, thus leading to electrochemical performance deterioration due to the loss of electrical contact within the particles and the detachment of the solid electrolyte interphase (SEI) from the surface [37]. In this regard, a recent report has shown that Na-alloying anodes based on micrometric size particles can deliver a reversible and stable reaction [35], although a recent work revealed relevant decrease in the Sn particles size during cycling independently from their initial shape [21]. These considerations have opened the debate on the optimal electrode architecture, which is also influenced by the choice of the polymeric binder due to its stabilizing role, as well as its potential for production/processing cost reduction, and environmental impact limitation [38]. Increasing the volumetric capacity of anodes based on HCs is currently a widely-investigated topic, however, issues including a low tap density and difficult calendering process are still affecting these interesting materials. Therefore, the significantly higher density of Sn compared to HCs appeared a favorable aspect to trigger SIBs towards energy density close to the threshold of LIBs [39,40]. Still, the minerals price and engineering state-of-art of metallic tin have both reached their asymptote, thus leaving only little room for improvements in cost. Indeed, as punctually discerned in a recent report, alloy-based anodes could be effective materials to lower the costs of SIBs in the next-future, although their broad diffusion may require enhancement of the cathode to keep the pace of LIBs and hold long-term competitivity [7].

1.3. An enhanced SIB configuration

Herein, we propose a highly-cyclable Na-ion full-cell by rationally combining enhanced cathode, anode and electrolyte materials to ensure a high capacity retention and stable galvanostatic cycling. The P2/P3-mixed layered-oxide cathode benefits from the incorporation of a small amount of Al^{3+} in the structure, which reinforces the stability toward the characteristic phase transitions of this class of materials [41–43]. Our approach can enable the realization of practical SIBs adopting P3/P2 class of layered-oxide cathodes, thus paving the way for further studies on this topic. Typical cathodes that deliver higher reversible capacity, such as those having O3 structure (i.e., the most diffused structure of Li-layered oxide cathode), are preferred since they can allow easier setup of the systems, in spite of pre-treatments may be still requested for allowing high cell efficiency [44–48]. However, the O3-type cathodes can face some problems, such as the poor symmetry of the crystal structure that may influence the electrochemical response of the native structure, since Na-ions diffuse through face-shared interstitial tetrahedral sites, while multiple phase transitions from O3 to O′3, P3, P′3, and P3″ can trigger an adverse effect on the cycling performance [49,50]. Moreover, the sodium extraction from the O3-phase can generate an increasing number of prismatic vacancies, resulting in the sliding of crystallite layers and culminating in the formation of thermodynamically stable P3-type phase [51]. On the other hand, P2-class cathode typically benefits from a larger Na layer spacing compared to the others, which can enhance the transport proprieties of Na^+, the rate performance, and the cycling stability of the electrode [52]. However, the large fraction of empty Na^+ ion sites in P2 layered materials can lead to inadequate Coulombic efficiency during the first charge/discharge cycle, with related issues on Na full-cell balancing. Hence, the synergic combination of the fast Na^+-ions diffusion of the P2-type material with the appropriate cycling stability exhibited by P3-type ones appeared to us of particular interest to enhance the electrochemical performance of the biphasic cathode [53–56]. Meanwhile, we demonstrated that chemical-sodiation can suitably allow the development of Na-ion energy storage systems using Na-deficient cathode, since the sodium content of the anode can be tuned by optimizing and controlling the sodiation procedure. We expect these findings to trigger renewed interest on mixed layered structured cathodes, often excessively overlooked in the past due to the lack of Na within their structure. The anode relies on nanometric tin particles incorporated into a buffering and highly-conductive carbon matrix [57]. The related slurry has been prepared by using CMC, which is a fluorine-free binder that allows for the aqueous processing to reduce manufacturing costs and increase the environmental compatibility [38]. In addition, the use of glyme-based electrolyte is suggested as a chemically stable alternative to the conventional carbonate-based solutions. The electrodes have been initially investigated in sodium half-cells to assess their performance in the proposed electrolyte medium, and then in full sodium-ion cells to determine the energy content, interphase properties, and electrochemical behavior. Finally, a thorough overview of the structural and

morphological evolution of the electrodes upon cycling is provided by *ex situ* X-ray diffraction and scanning electron microscopy.

2. Experimental section

2.1. Electrode materials

The $Na_{0.48}Al_{0.03}Co_{0.18}Ni_{0.18}Mn_{0.47}O_2$ (NCAM) cathode material consisting of 79 vol% P3-type (space group *R3m*, No. 16) and 21 vol% P2-type (space group $P6_3/mmc$, No. 194) structures was synthesized through a co-precipitation route and calcination at 1000 °C following an optimized method reported in previous works [42,43]. The tin-carbon (Sn-C) anode with a Sn to C weight ratio of 35:65 was synthetized as previously reported via resorcinol-formaldehyde jellification, impregnation with an organometallic tin precursor, and annealing under Ar/H_2 (95/5 vol%) at 700 °C [58].

2.2. Electrode preparation

The electrode slurries were prepared in a mortar by dispersing the active material powder, either NCAM or Sn-C, carbon black (Super P carbon, SPC, Timcal), and either polyvinylidene fluoride (PVdF 6020, Solef) or CMC (average molecular weight 700 000, Sigma-Aldrich) as binder for the cathode and anode tapes, respectively. The three components were mixed in the 8:1:1 wt ratio and dispersed either in *N*-methyl-2-pyrrolidone (NMP, Sigma-Aldrich) for the cathode, or in deionized H_2O for the anode achieving a 2.5 wt% CMC solution. The obtained slurries were cast by a doctor blade tool on either aluminum foil (thickness of 15 μm, MTI Corporation) for NCAM or copper foil (thickness of 10 μm, MTI Corporation) for Sn-C and subsequently dried at 70 °C inside a climatic chamber equipped with a peristaltic pump. The tapes were subsequently calendared by using an MSK-2150 Rolling Machine (MTI Corp.) to achieve thickness values within the range from 80 to 100 μm for the anode (about 60 % of the initial thickness) and in the range from 70 to 90 μm for the cathode (about 70 % of the initial thickness). Afterwards, the tapes were cut into discs of 10 and 14 mm-diameter (electrode geometric area of 0.785 and 1.54 cm^2, respectively) and dried for 2 h at 110 °C under vacuum inside a Büchi oven to remove possible traces of H_2O and NMP before transfer in an Ar-filled glovebox (MBraun, H_2O and O_2 below 0.5 ppm). Additional slurries of anode and cathode were prepared with the same procedure as above, however with different thicknes. Therefore, the active material loading ranged within 3.5 and 7.6 $mg_{Sn\text{-}C}$ cm^{-2} and within 1.5 and 11.5 mg_{NCAM} cm^{-2}. The specific values are indicated in the corresponding figure panels. A SPC:PVdF electrode was also prepared with a 80:20 wt ratio, using NMP as solvent, and casting the slurry onto Al. After drying and calendaring, the electrode tape was cut into discs of 10 mm- diameter and later employed for the electrolyte electrochemical stability test. The sodiated state of the Sn-C electrodes $(Na_xSn\text{-}C)_{minutes}$ was obtained inside an Ar-filled glove box via capillary contact between the pristine Sn-C electrode and sodium metal by applying a weight of 0.2 kg at the electrode surface for a certain time. Prior to the contact, the sodium metal foil was soaked with the electrolyte solution, that is, sodium hexafluorophosphate as the conducting salt ($NaPF_6$, 99.9 % trace metals basis, anhydrous, battery grade, Sigma-Aldrich) dissolved in diethylene glycol dimethyl ether (DEGDME, $CH_3(OCH_2CH_2)_2OCH_3$, Sigma-Aldrich) in a 1 mol_{salt} $dm^{-3}_{solvent}$ (1 M concentration). Prior to use, DEGDME was stored in dry molecular sieves (0.3 nm, rods, ~1.6 mm diameter, Sigma- Aldrich) for one week to remove H_2O, the content of which was verified to be below 10 ppm by an 899 Karl Fischer Coulometer (Metrohm). Three sodiation times were evaluated, that is, 15, 27 and 30 min, and the obtained electrodes have been indicated as $(Na_xSn\text{-}C)_{15min}$, $(Na_xSn\text{-}C)_{27min}$ and $(Na_xSn\text{-}C)_{30min}$.

2.3. Material characterization

X-ray diffraction (XRD) was performed by scanning the 10°–60° 2θ range on the pristine Sn-C anode with step size of 0.02° and rate of 10 s $step^{-1}$, using a Bruker D8 Advance instrument equipped with a Cu Kα radiation source (8.05 keV). Thermogravimetric analysis (TGA) was performed on the pristine CMC powder, and the aqueous CMC solution between 25 and 800 °C, with a heating rate of 5 °C min^{-1} by a Mettler-Toledo TGA 2 instrument (Mettler-Toledo, Columbus, OH, USA) under a dry air flow.

2.4. Na half-cells characterization

Three-electrode Swagelok-type T-cells using 10 mm-diameter electrodes and CR2032 coin-type cells (MTI Corp.) using 14 mm-diameter electrodes were assembled inside an Ar-filled glovebox by stacking a sodium metal disc (99.9 % trace metal basis, Sigma-Aldrich) as counter/reference electrode, a 10 or 16 mm glass fiber (Whatman GF/B) disc as separator soaked with the DEGDME 1 M $NaPF_6$ electrolyte (50 l and 200 μl for coin- and Swagelok-type cells, respectively), and either Sn-C, $(Na_xSn\text{-}C)_{min}$, or NCAM as working electrode. The electrolyte stability toward oxidation was determined through inert-electrode Linear-Sweep Voltammetry (LSV) carried out in three-electrode Swagelok-type T-cell using Na as reference electrode and a SPC-based working electrode, with a scan rate of 0.1 mV s^{-1} from the open circuit voltage (OCV) to 5 V. The electrochemical processes and the electrode/electrolyte interphases of Sn-C and NCAM were investigated through cyclic voltammetry (CV) and electrochemical impedance spectroscopy (EIS) in three-electrode Swagelok-type T-cells employing a VersaSTAT MC Princeton Applied Research (PAR-AMETEK) multichannel potentiostat. CV was performed within the 0.01–2.0 V *vs.* Na^+/Na and 1.2–4.2 V *vs.* Na^+/Na potential ranges for Sn-C and NCAM, respectively, at a scan rate of 0.1 mV s^{-1}, while EIS measurements were collected at the OCV condition before cycling, and upon 1 and 5 CV runs, using an alternate voltage signal of 10 mV in the frequency range between 500 kHz and 100 mHz. Rate capability test on the pristine Sn-C anode was performed by galvanostatic cycling in Na half-cell between 0.01 and 2.0 V, applying specific currents increasing every 10 cycles from 0.05 A g^{-1} to 0.10, 0.20, 0.30, 0.60, and 1.2 A $g^{-1,}$ before decreasing it back to 0.05 A g^{-1} at the 61st cycle. The chemical pre-sodiation of the anode was investigated by galvanostatic cycling $Na||(Na_xSn\text{-}C)_{min}$ half-cells between 0.01 and 2.0 V at the constant current rate of 0.05 A g^{-1}, the sodiation degree (x) related to the 27 min sodiation protocol was estimated through galvanostatic and potentiostatic methods. The galvanostatic test was carried out in 2-electrode cell, by applying a current of 0.05 A g^{-1} from the OCV of the $Na||(Na_xSn\text{-}C)_{27min}$ cell to 2.0 V. The potentiostatic test was a coulometry performed in 3-electrode cell by holding the potential at 0.5 V *vs.* Na^+/Na for 5 h and 20 min, acquiring the current each 3 s. To assess the Na-plating risk window, the 2-electrode half-cell used to estimate the sodiation degree was galvanostatically discharged using a current of 0.05 A g^{-1} held for 8 h. Na||NCAM half-cells were galvanostatically cycled either in the 1.4–4.2 V voltage range at the constant current rate of 0.05 A g^{-1}, or limiting the voltage window between 1.4 and 4.0 V at a constant specific current of either 0.05 A g^{-1} or 0.1 A g^{-1}. The lifetime/energy trade-off in the 1.4–3.9/4.0/4.1/4.2 V voltage range was investigated by galvanostatically cycling 3-electrode Na||NCAM Swagelok-type T-cell at 0.05 A g^{-1}, while acquiring EIS spectra at the end of the 1st, 5th, 10th, and 50th discharge. The average discharge voltage (i.e., the *mean voltage*) was considered as the performance-indicator of this test. To assess the interplay between electrolyte decomposition, magnitude of applied current, and NCAM side feature at high-voltage, two Swagelok-type T-cells (2-electrode configuration without Na reference) were galvanostatically cycled either at 0.05 A g^{-1} or 0.12 A g^{-1} between 1.2 and 4.4 V. All the galvanostatic cycling tests, except for the former one, were carried out in CR2032 coin-type cells using a MACCOR series 4000 battery tests instrument either at 25 or 30 °C (see specific values in the corresponding figure captions).

2.5. Full-cells characterization

(Na_xSn-C)$_{27min}$||NCAM full-cells were assembled by using a negative to positive ratio (N/P) between 1.1 and 1.3, as determined by considering the initial capacity achieved by the electrodes in the respective Na half-cells, e.g., 1.19 mAh cm^{-2} for NCAM during discharge (Na-intercalation) and 1.53 mAh cm^{-2} for (Na_xSn-C)$_{27min}$ during charge (Na-dealloying), with active material mass loadings of 7.5 mg cm^{-2} and 6.2 mg cm^{-2}, respectively. The full-cells were assembled by stacking one (Na_xSn-C)$_{27min}$ electrode, one glass fiber (Whatman GF/B) disc as separator soaked with the DEGDME 1 M $NaPF_6$ electrolyte (50 μl) and one NCAM electrode. The specific capacity, as well as the specific current, is referred to the cathode active material mass. The (Na_xSn-C)$_{27min}$ and NCAM capacity values for the N/P determination were evaluated by galvanostatic cycling of the corresponding Na half-cells either between 0.01 and 2.0 V at 0.05 A g^{-1} for (Na_xSn-C)$_{27min}$, or between 1.4 and 4.4 V at 0.05 A g^{-1} for NCAM. The electrochemical performance of the (Na_xSn-C)$_{27min}$||NCAM full-cell was evaluated through galvanostatic cycling in the 0.8–4.2 V voltage range either at the 0.05 A g^{-1} or 0.10 A g^{-1} constant current rate (referred to the NCAM mass), or in the restricted 0.8–4.0 V and 0.8–3.9 V voltage ranges at 0.05 A g^{-1}. For the latter test, a potentiostatic step was adopted at 3.9 V at the end of every charge until the current decreased to 0.0125 A g^{-1}. The rate capability test was carried out in the 0.8–4.1 V voltage range by applying specific currents increasing every 5 cycles from 0.05 A g^{-1} to 0.10, 0.15, 0.20, and 0.25 A g^{-1} before lowering it back to 0.05 A g^{-1} at the 26th cycle. The energy density of this test was reported considering either the cathode active material content (NCAM) or both anode plus cathode (namely NCAM and Sn-C). The current rate capability test was carried out without using potentiostatic steps. An additional normalization of the energy density (Wh kg^{-1}) of the full-cells has been carried out by taking into account full electrode masses and stack with separator/electrolyte for possibly enabling preliminary benchmarking of the laboratory-scale cells. EIS spectra were collected using an alternate voltage signal with an amplitude of 10 mV between 500 kHz and 20 mHz at the OCV and in the discharged state after the rate capability test. After the above test, the full-cell was also subjected to CV within the 0.8–4.2 V *vs.* Na^+/Na potential range using a scan rate of 0.1 mV s^{-1}. All the EIS plots were fitted using the non-linear least squares (NLLS) method with the aid of the Boukamp software by accepting only fits with a χ^2 value of the order of 10^{-4} or lower [59,60]. All the galvanostatic cycling of the full-cells were carried out in CR2032 coin-type cells, while the rate capability test combined with EIS, SEM and CV was carried out in a 3-electrode Swagelok-type T-cell. The galvanostatic cycling tests were performed using a MACCOR series 4000 battery tests instrument either at 25 or 30 °C (see specific values in the corresponding figure captions). The EIS and CV tests employed a VersaSTAT MC Princeton Applied Research (PAR-AMETEK).

2.6. Ex situ analyses

The (Na_xSn-C)$_{27min}$ and NCAM electrodes were investigated by XRD after 100 galvanostatic charge/discharge cycles in (Na_xSn-C)$_{27min}$||NCAM full-cells at 0.05 A g^{-1} in the 0.8–4.0 V voltage range. The XRD data were acquired in the 10°–80° 2θ range through a Bruker D8 Advance instrument equipped with a Cu Kα radiation source using a step size of 0.02° and rate of 10 s per step. Scanning electron microscopy (SEM) of a (Na_xSn-C)$_{27min}$ electrode retrieved from a cycled full-cell was performed using a ZEISS Crossbeam XB340 microscope operating with an accelerating voltage of 5 kV in secondary electrons mode. To avoid external contamination, the electrode was transferred from the Ar-filled glove box to the microscope with the aid of a sealed transfer box. Prior to all the *ex situ* analyses, the cells were recovered at the discharged state and disassembled inside the Ar-filled glove box, and the retrieved electrodes were washed with a few drops of DEGDME and dried under vacuum at room temperature. The (Na_xSn-C)$_{27min}$ electrode morphology and elemental distribution were investigated by means of SEM-Energy Dispersive X-ray Spectroscopy (SEM-EDS) using a Zeiss EVO 40 relying on a LaB_6 thermionic gun in secondary electrons mode operating at 5 kV. EDS elemental maps were collected on the SEM secondary electrons images via an X-ACT system associated with the SEM equipment.

3. Results and discussion

3.1. Characteristics and performance of the Sn-C anode in Na half-cells

As mentioned above, the Sn-C electrode is achieved by using water as casting-solvent and CMC as binder in order to lower down the overall price and mitigate possible health/environmental issues caused by fluorinated binders and organic solvent [38]. Therefore, a thorough investigation is certainly requested in addition to that previously reported in literature to check the stability of the nanostructured Sn-C in the new environment [58]. Initially, the thermal proprieties of the CMC binder are investigated through TGA upon heating from 25 °C to 800 °C under dry air flow, either in the pristine state (i.e., material powder) or in the H_2O 2.5 % CMC solution used for the slurry preparation. The thermograms and respective derivate curves are reported in Fig. 1a, which shows for the dry CMC three main oxidation/decomposition steps indicated by the derivative peaks centered at 280 °C, 310 °C, and 400 °C, while the process at 120 °C is attributed to the loss of trapped water/-moisture within the CMC structure. The same test carried out on the aqueous CMC solution displays the expected weight loss at 120 °C due to the removal of the water, until reaching ~2.5 % of the initial weight, that is, a value matching the nominal CMC content. Interestingly, the water removal occurs through various steps, indicating the formation of solvation structures with the CMC. The stability of the nanometric Sn particles toward possible oxidation to SnO_2, triggered by water during electrode preparation and drying, is assessed via XRD.

The diffractogram of the dry Sn-C electrode in Fig. 1b indicates the absence of additional phases, beside the ones related to Sn and to the Cu current collector (reference data from ICSD #40038 and #627114, respectively). These outcomes indicate the relevant stability of the active material during water processing, while the broad wave detected between 20 and 30° originates from the carbon matrix hosting the nanometric Sn particles, and possibly from the amorphous CMC binder whose diffractogram is also reported for better comparison in Fig. 1b [61,62].

Fig. 2 reports the electrochemical response of the Sn-C electrode in Na half-cell achieved by performing CV and EIS. The voltammograms in Fig. 2a reveal during the first cathodic scan a current onset below 0.6 V *vs.* Na^+/Na, due to the beginning of Na-Sn alloy formation and the concomitant insertion of Na into the amorphous carbon matrix until 0.01 V *vs.* Na^+/Na [63]. This voltammetric wave appears partially irreversible, mostly due to the side reduction of the electrolyte which typically leads to the formation of a protective SEI layer at the electrode surface [64]. Different kinetics for the oxidation processe compared to the reduction one are indicated by the first anodic scan, which shows a more resolved signal evolving by a series of peaks extending from 0.15 to 0.66 V *vs.* Na^+/Na, due to the Na-Sn dealloying below 0.5 V *vs.* Na^+/Na, and to the deinsertion of Na from the carbon at higher values [65]. The signal related to the irreversible electrolyte reduction remarkably decreases at the second cathodic scan, and almost fully vanishes during the subsequent cycles which exhibit exclusively a voltage slope with onset below 0.4 V *vs.* Na^+/Na. Instead, the anodic profiles show the above discussed oxidation peaks, which appear well defined between 0.1 and 0.7 *vs.* Na^+/Na during the whole CV test. These results substantially differ from previous literature on Sn-based anodes for SIBs, which reported the presence of one or more additional peaks upon the cathodic scan in the region between 0.1 and 0.8 V *vs.* Na^+/Na, thus suggesting possible influence of the binder nature, the characteristic electrode structure, and its morphology on the Na–Sn alloying

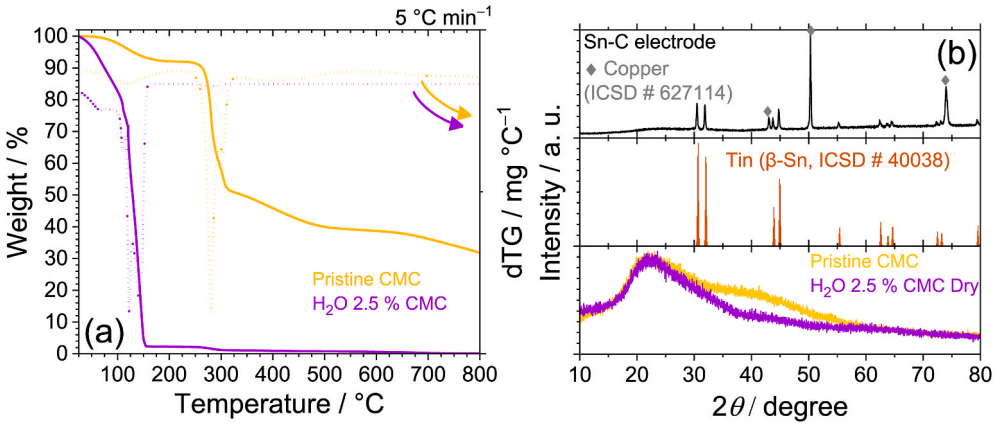

Fig. 1. Physicochemical features of the Sn-C electrode and CMC binder, in detail: **(a)** TGA of pristine CMC binder and of H_2O 2.5 % CMC solution, and corresponding DTG curves (dotted lines); **(b)** X-ray diffractograms of the Sn-C electrode, and of the CMC binder at the pristine state and after drying its H_2O solution. Reference data for Sn (β-Sn, ICSD # 40038) and Cu (ICSD # 627114) are reported for comparison.

kinetics [66–69]. By the ongoing of CV, the current intensity raises for the anodic process at 0.21 V *vs.* Na^+/Na, fluctuates for the one at 0.28 V *vs.* Na^+/Na, while decreases for the processes over 0.5 V *vs.* Na^+/Na. The modification in current response of the Na–Sn dealloying processes indicates the variation of the corresponding kinetics, likely due to the consolidation of the SEI layer and stabilization/rearrangement of the hosting carbon matrix upon repeated cycling, which favor the low-voltage processes (<0.5 V *vs.* Na^+/Na) and limit the cell polarization [64]. In addition, the improvement of the profiles overlapping upon repeated scans suggests the progressive stabilization of the electrochemical process, thus indicating the effectiveness of the Sn-C nanostructure in buffering the volume variations associated to the Na–Sn (de) alloying to avoid structural degradation of the electrode. The EIS graphs in Fig. 2b, recorded at the OCV condition of the cell and after 1 and 5 CV scans, evidence an overall decrease of the electrode/electrolyte interphase resistance upon cycling, thus further suggesting the above-mentioned enhancement. The NLLS analysis of the Nyquist plots allows for the evaluation of resistive and capacitive components of the cells through the description of the frequency-dispersion spectra with the equivalent circuit $R_e(R_nQ_n)Q_w$, where: *i)* R_e defines the electrolyte bulk resistance obtained by high frequency intercept of the plot; *ii)* the (R_nQ_n) elements (with $n = 1, 2, \ldots$) account for the electrode/electrolyte interphase phenomena, including possible charge transfer processes and SEI formation, identified by high-middle frequency semicircles the width of which allows the determination of the total interphase resistance ($R_I = R_1 + R_2 + \ldots$); *iii)* Q_w is a constant phase element (CPE) represented by the tilted line at low-frequency values that describes the semi-infinite Warburg-type Na^+ ion diffusion [59,60]. Table 1 summarizes the NLLS results and reveals an interphase resistance value of about 53 Ω at the OCV, that decreases to 8 Ω after the first cycle, and stabilizes around the same value after 5 CV scans. The table also shows the modification of the equivalent circuit after 1 cycle and the decrease of the (R_nQ_n) elements number. The remarkable decrease of the resistance upon CV, and the reduction of the circuital elements number are in line with the modification of the electrode/electrolyte interphase discussed above, which improves the conductivity and the reaction kinetics by the ongoing electrochemical process.

Fig. 3 summarizes the galvanostatic cycling performances of the Sn-C electrode in sodium half-cell. A rate capability test is initially performed

Table 1
NLLS analysis carried out on the Nyquist plots displayed in Fig. 2b recorded on a three-electrode Na||Sn-C half-cell at the OCV and after 1 and 5 CV runs.

Cell condition	Circuit	R_1 [Ω]	R_2 [Ω]	R_3 [Ω]	$R_I = \sum R_n$ [Ω]	χ^2
OCV	$R_e(R_1Q_1)(R_2Q_2)(R_3Q_3)Q_w$	42.5 ± 7.1	7.2 ± 2.9	3.3 ± 0.4	53.0 ± 5.4	2×10^{-5}
After 1 cycle	$R_e(R_1Q_1)Q_w$	7.5 ± 0.5	/	/	7.5 ± 0.5	4×10^{-4}
After 5 cycles	$R_e(R_1Q_1)Q_w$	7.8 ± 0.7	/	/	7.8 ± 0.7	2×10^{-4}

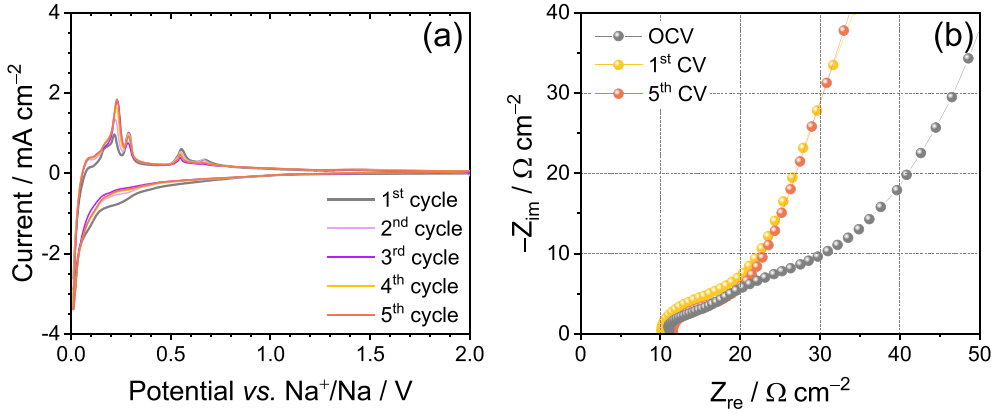

Fig. 2. **(a)** CV profiles and **(b)** Nyquist plots recorded by EIS upon CV on a Na||Sn-C half-cell; CV potential range: 0.01–2.0 V *vs.* Na^+/Na, scan rate: 0.1 mV s^{-1}, EIS performed at the OCV cell condition, and after the 1st and 5th CV scan between 500 kHz and 100 mHz using an alternating voltage signal with an amplitude of 10 mV. Temperature: 25 °C.

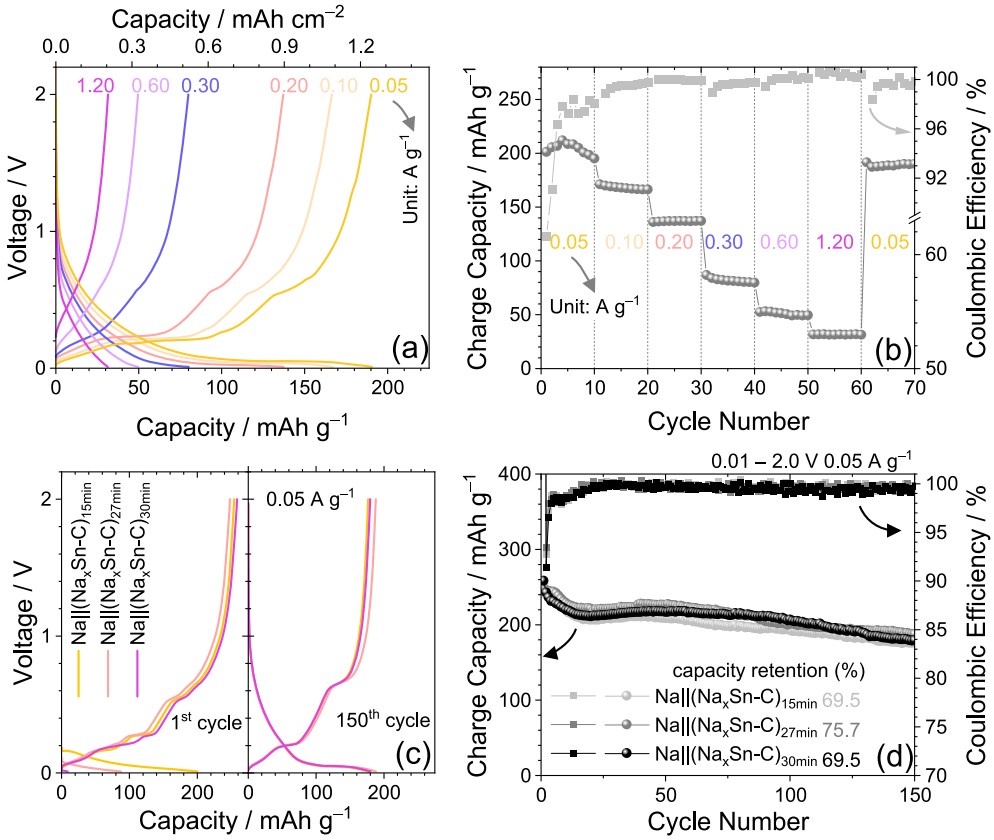

Fig. 3. **(a, b)** Galvanostatic cycling performance upon rate capability test of a Na||Sn-C half-cell in terms of **(a)** selected voltage profiles (10th cycle for each current rate) and **(b)** corresponding charge capacity *vs.* cycle number trend; **(c, d)** galvanostatic cycling performance of Na||$(Na_xSn\text{-}C)_{min}$ half-cells tested at 0.05 A g^{-1} using Sn-C electrodes chemically sodiated for either 15, 27, or 30 min reported in terms of **(c)** 1st (left-hand panel) and 150th (right-hand panel) voltage profile, and **(d)** corresponding charge capacity *vs.* cycle number trends. Right *y*-axes in panels **(b)** and **(d)** reports Coulombic efficiency; voltage range: 0.01–2.0 V; electrode geometric area: 1.54 cm^2; active material mass loading: 6.0–6.8 mg cm^{-2}. Temperature: 25 °C.

by increasing the current every 10 cycles from 0.05 A g^{-1} to 0.10, 0.20, 0.30, 0.60, and 1.20 A g^{-1}, with selected voltage profiles in Fig. 3a and the corresponding charge capacity trend in Fig. 3b. The first cycle of this test at 0.05 A g^{-1} reported in Fig. S1 (Supporting Information) evidences the irreversible capacity expected by electrolyte decomposition, SEI formation, and electrode reorganization, that leads to an initial Coulombic efficiency of 61.5 %. Instead, the voltage profile after 10 cycles at the same current reveals an efficiency approaching 100 %, and a reversible electrochemical process centered between 0.2 and 0.8 V, evolving by a single sloped profile during discharge and various merged plateaus during charge, as already observed during the CV (compare Fig. 3a with Fig. 2a). The curves of Fig. 3a also show a moderate decrease in terms of delivered capacity alongside a slight increase of the overpotential upon current increase, due to the increasing ohmic polarization. Indeed, the charge capacity *vs.* cycle number trend displayed in Fig. 3b exhibits a maximum capacity of 212 mAh g^{-1} achieved at 0.05 A g^{-1}, and values of 166, 137, 80, 50, and 32 mAh g^{-1} at 0.10, 0.20, 0.30, 0.60, and 1.20 A g^{-1}, respectively. In addition, the electrode recovers 89.6 % of the initial capacity after decreasing the current rate back to 0.05 A g^{-1} at the 61st cycle, thus suggesting remarkable structural stability upon cycling at high currents. The trend of Fig. 3b also evidences a progressive improvement of the delivered capacity during the initial stages of the test, which is accompanied by an increase of the Coulombic efficiency from 61.5 % at the first cycle to a value around 99 % upon 10 galvanostatic cycles. This activation process is likely justified by the progressive improvement of the electrode/electrolyte interphase previously observed by CV and EIS. On the other hand, a fast enhancement of the cell efficiency is crucial to avoid a relevant consumption of the cyclable Na, which may potentially undermine the performance of the full-cell especially in presence of a sodium-deficient cathode such as the one adopted in this study ($Na_{0.48}Al_{0.03}Co_{0.18}Ni_{0.18}Mn_{0.47}O_2$, or NCAM) [42]. Taking into account this limitation, the pre-sodiation of the Sn-C anode through direct contact with sodium metal, *i.e.*, chemical sodiation, is selected as viable method to ensure a sufficient sodium reservoir in the full-cell setup using the NCAM cathode [70]. The control of the contact time between Sn-C and Na metal, the applied pressure, and the content of active material in the electrode play fundamental role during pre-sodiation. The above conditions are crucial for regulating the sodium content into the anode, which must provide a sufficient amount of cyclable Na to balance the full-cell, and avoid at the same time an excess that can trigger undesired metal plating during charge [70]. Other pre-sodiation strategies not considered in this work rely on the use of sacrificial salts and/or additives within the cell, however with additional processing steps that may lead to gas evolution upon cell operation [26,71–75]. Therefore, the chemical sodiation of the Sn-C electrode is evaluated herein by tuning the contact time, as evidenced by Fig. 3c, which shows the voltage profile at the first (left-hand side) and 150th (right-hand side) cycles of Na half-cells studied at 0.05 A g^{-1} using Sn-C electrodes chemically sodiated for either 15, 27, or 30 min. All cells show a higher capacity during charge than during discharge in the first cycle, rather than the typical behavior in which the discharge exceeds the charge observed for the cell using the pristine Sn-C (compare Fig. 3c and Fig. S1). In addition, the data indicate for the pre-treated electrodes the absence of the irreversible shape typically ascribed to the electrolyte reduction, and evidence a higher capacity upon charge compared to pristine Sn-C, that is, around 250–260 mAh g^{-1} instead of 212 mAh g^{-1}. These outcomes suggest an effective pre-sodiation triggered by the contact time, and possible over-sodiation

at the electrode surface due to the excess charge capacity, which appears not detrimental for the anode stability as demonstrated by the corresponding cycling trend in Fig. 3d [76]. It is worth mentioning that the cell using the $(Na_xSn\text{-}C)_{15min}$ still delivers around 200 mAh g^{-1} during first discharge, thus indicating an insufficient sodiation degree achieved using 15 min of contact to get a suitable balancing of the full-cell with the Na-deficient NCAM. On the other hand, the cell using $(Na_xSn\text{-}C)_{30min}$ shows less than 20 mAh g^{-1} during first discharge, thus achieving almost full sodiation of the Sn-C after 30 min of contact with Na. The latter excessive sodiation may lead to alkali metal deposition during Na-ion full-cell charging, although it may represent a viable pathway in view of a possible application in Na metal-free sulfur-based full-cells [63]. On the other hand, the $(Na_xSn\text{-}C)_{27min}$ delivers 90 mAh g^{-1}, which is expected to counterbalance the NCAM capacity even considering its Na-deficiency. Therefore, we may indicate 27 min as the most adequate timeframe within our pre-sodiation conditions to achieve efficient Na-ion cell. The trends in Fig. 3d evidence for the cells using the pre-sodiated electrodes a retention ranging from 70 % to 76 % over 150 cycles, which is also demonstrated by the voltage profile of the last cycle in Fig. 3c (right-hand panel). Furthermore, the pre-sodiated electrodes show a faster interphase activation compared to the pristine Sn-C electrode, since the related Na half-cells reach a Coulombic efficiency higher than 99 % far faster (compare Fig. 3b and d).

The chemical sodiation triggered by mechanical contact between Na foil and the electrode wet by the electrolyte allows a rapid and efficient activation of the material, and represents a viable strategy for achieving Na-ion batteries exploiting alloying negative electrodes [70,77]. The development of new battery configurations based on electrode pre-sodiation by capillary diffusion requires an adequate tuning of the contacting time, to ensure a Na-amount in the anode sufficient to fully allow the electrochemical reaction at the cathode. The activation protocol for the Sn-C electrode with contact time of 27 min is selected as suitable for Na-ion cell application, and therefore electrochemically investigated hereafter by means of galvanostatic and potentiostatic techniques, as well as morphologically using *ex-situ* SEM-EDS analysis to determine the actual Na content in the $(Na_xSn\text{-}C)_{27min}$ electrode. Fig. 4a indicates a delivered capacity upon galvanostatic charge of the Na||$(Na_xSn\text{-}C)_{27min}$ cell using a current of 0.05 A g^{-1} between the OCV and 2.0 V corresponding to 268.0 mAh g^{-1}, in accordance with the result presented in Fig. 3. Fig. 4b shows the potentiostatic polarization (coulometry) extended to a timeframe comparable with that of the previous galvanostatic experiment. Hence, a sodiation degree in $(Na_xSn\text{-}C)_{27min}$ of $x = 0.5$ is calculated by taking into account the overall extracted capacity ($\varepsilon = 2.828$ C), the Faraday constant (F = 96485 C mol^{-1}), the mass of Sn-C in the electrode ($m = 2.872 \times 10^{-3}$ g), and its molar weight with the $Sn_{0.35}C_{0.65}$ chemical formula ($M_{Sn\text{-}C} = 49.355$ g mol^{-1}), using the equation: $x = \frac{\varepsilon \times M_{Sn-C}}{F \times m}$. The plating-risk window analysis represents a key-factor, which determines the safety level of the anode in a Na-ion device [78,79]. To assess this aspect for the $(Na_{0.50}Sn\text{-}C)_{27min}$ electrode, the half-cell of Fig. 4a is over-discharged for 8 h using a current of 0.05 A g^{-1} without imposing any voltage limit, and the result are reported in Fig. 4c (inset shows a magnification of the onset for Na-nucleation). This test suggests that the anode has a tolerance of 13 mAh g^{-1} over its theoretical capacity (*i.e.*, 271 mAh g^{-1} for $Sn_{0.35}C_{0.65}$) before occurring of Na-plating, thus allowing the estimation of ±5 % of possible N/P fluctuation without compromising the safe Na-ion full-cell operation. Importantly, the Na distribution across the electrode upon chemical sodiation is accounted by means of SEM-EDS analysis in Fig. 4d–g. The elemental maps distributions of Na and Sn, respectively reported in Fig. 4d and e, suggest that the sodiation protocol related to 27 min yields to a uniform sodiation of the $(Na_{0.50}Sn\text{-}C)_{27min}$ electrode, without relevant clusters of metallic Na or considerable damage. To further verify the sodiation degree (x), the atomic ratio of Na and Sn in the $(Na_xSn\text{-}C)_{27min}$ electrode is accounted by sampling EDS spectrum in various portions (the spectra of some representative spots are reported in Fig. 4f and g). Remarkably, x is estimated to range from 0.67 to 0.36, with average value of 0.52, which agrees with the coulometry estimation of Fig. 4b, despite the error derived from the presence of Na in the CMC binder, as well in possible $NaPF_6$ salt residue.

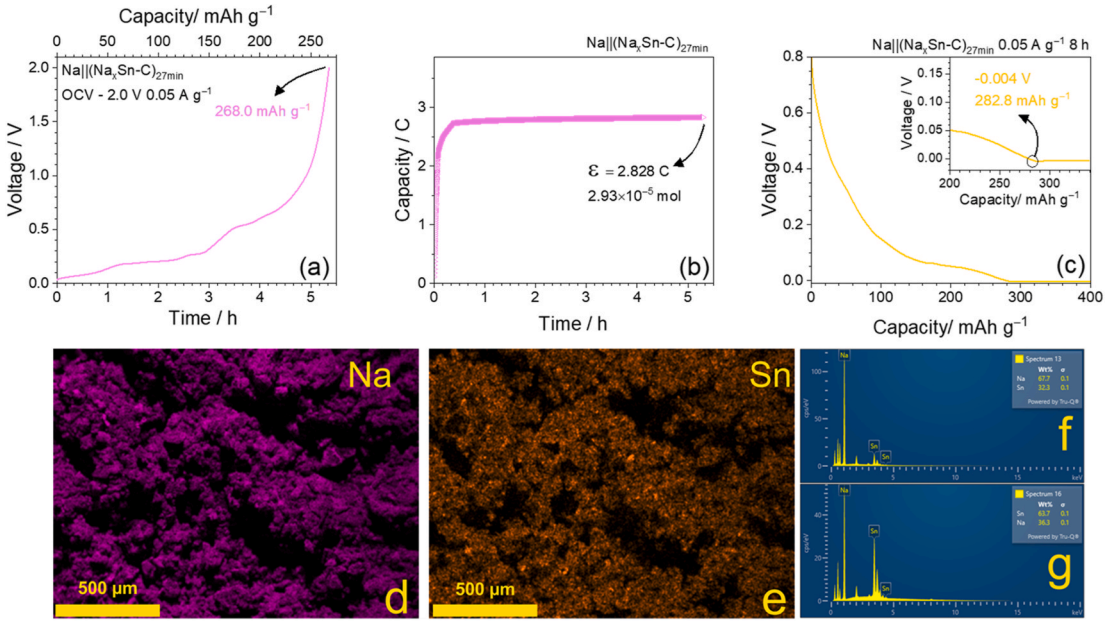

Fig. 4. Estimation of Na content across the $(Na_xSn\text{-}C)_{27min}$ electrode through electrochemical methods and SEM-EDS investigation, and determination of its Na-plating window, in detail: **(a)** galvanostatic charge of Na||$(Na_xSn\text{-}C)_{27min}$ half-cell reported in terms of first charge profile (6.1 ± 0.1 mg of Sn-C, 14 mm-diameter electrode); **(b)** coulometry test (chronocoulometry at 0.5 V *vs.* Na^+/Na, 1 point collected each 3 s, 5 h and 20 min timeframe) to assess the sodiation degree x in $(Na_xSn\text{-}C)_{27min}$ electrode (2.9 ± 0.1 mg of Sn-C, 10 mm-diameter electrode, test carried out in Swagelok-type T-cell); **(c)** plating test carried out using the half-cell of panel (a) to assess the allowed fluctuation of the N/P ratio before Na-plating; **(d, e)** SEM-EDS elemental maps distribution, related respectively to Na and Sn, and **(f, g)** related spectra.

3.2. Characteristics and performance of the NCAM cathode in Na half-cells

The NCAM cathodes were prepared and studied in previous work using a carbonate-based electrolyte [42], which offered relevant stability towards oxidation and allowed for the investigation of high-voltage features of the electrochemical process [80]. Lately, great attention has been devoted to glyme-based electrolytes relying on solvents with $CH_3(OCH_2CH_2)_nOCH_3$ general formula due to their relevant Na^+ solvation capability and transport properties, as well as adequate viscosity and dielectric constant, particularly for low n values that ensure high Na^+ conductivity [12]. However, their stability towards oxidation is usually limited to potential values below 4.5 V *vs.* Na^+/Na, which can hinder their application in batteries using high voltage cathodes. Herein, the DEGDME 1 M $NaPF_6$ electrolyte solution is exploited due to the promising performance demonstrated in other systems [81–83], although a thorough investigation to assess its compatibility with the NCAM cathode is still needed. Therefore, the electrochemical process and electrode/electrolyte interphase of the of NCAM in DEGDME 1 M $NaPF_6$, as well as its cycling response in Na half-cells, are investigated by CV, EIS, and galvanostatic cycling, and the results are reported in Fig. 5. The voltammetry curves (Fig. 5a) reveal a reversible electrochemical Na^+ (de)intercalation process, characterized by several peaks occurring within the 1.2 − 4.2 V *vs.* Na^+/Na potential range. It is worth mentioning that the first anodic scan (black curve in Fig. 5a) starts from a potential of about 3.1 V *vs.* Na^+/Na, i.e., a high value indicating for the pristine NCAM material a partially charged state, which is in line with the sodium content below 0.5 equivalents in its stoichiometry. As the voltammetry scan begins, two resolved oxidation peaks appear at about 3.2 and 3.4 V *vs.* Na^+/Na, attributed to the Ni^{4+}/Ni^{2+} couple, followed by two merged peaks at 3.7 and 3.8 V *vs.* Na^+/Na ascribed to the Co^{4+}/Co^{3+} couple, and by a current increase with an onset at 4.1 V *vs.* Na^+/Na likely due to possible phase transition including partial electrolyte oxidation [43,84]. The first cathodic scan shows the partial reversibility of the latter process, with a first reduction signal slightly below 4.1 V *vs.* Na^+/Na, two reversible peaks ascribed to the Co^{4+}/Co^{3+} couple merged at ~3.7 V *vs.* Na^+/Na, and those associated to the Ni^{4+}/Ni^{2+} couple at 3.3 and 3.2 V *vs.* Na^+/Na, all with a very modest polarization and remarkable symmetry compared to the oxidation ones. By the ongoing of the first cathodic scan, the CV reveals the appearance of reduction waves approximately at 2.7 V, 2.3 V, and below 2.0 V *vs.* Na^+/Na associated to the Mn^{4+}/Mn^{3+} redox process, which are reversed during the second and the subsequent anodic scans into a single broad peak extended from 1.8 to 2.9 V *vs.* Na^+/Na [43,84]. In spite of a minor signal decrease above 4.1 V, all the described oxidation and reduction signals are almost fully reproduced throughout the whole CV test, with more defined peaks compared to those observed in previous work using a carbonate-based electrolyte [13,42,85]. Hence, the CV response of Fig. 5a suggests that the kinetics associated with the ion motion within the layered electrode structure can be promoted into a more efficient way by the glyme-based electrolyte rather than the carbonate-based one. Furthermore, the almost full overlapping of the voltammograms during the whole test indicates a relevant reversibility in the glyme-based electrolyte of the NCAM electrochemical process, which can proceed without significant modification or gliding of the layers into the material, and with minor structural reorganization due to sodium vacancy ordering. The electrode/electrolyte interphase changes occurring during CV are monitored by performing EIS, as illustrated by the corresponding Nyquist plots in the inset of Fig. 5a. The data reflect the contribution of several resistive and pseudocapacitive elements, arranged in the equivalent circuit depicted in Table 2 along with the corresponding NLLS fitting results. The various elements account for the electrolyte resistance at high frequencies, the interphase resistance including the Na^+ diffusion across the SEI and the charge transfer processes at intermediate frequencies, as well as the Na^+ diffusion within the NCAM lattice at low frequencies. The NLLS results show a relatively low electrode/electrolyte interphase resistance at the OCV, that is, 151 Ω, which decreases to 112 Ω upon discharge to 1.2 V *vs.* Na^+/Na due to the concomitant increase of the NCAM conductivity promoted by full-sodiation. The resistance increases back to 166 Ω at the discharged state after 5 cycles, in part due to NCAM de-sodiation with conductivity decrease, and in part due to the marginal electrode passivation induced

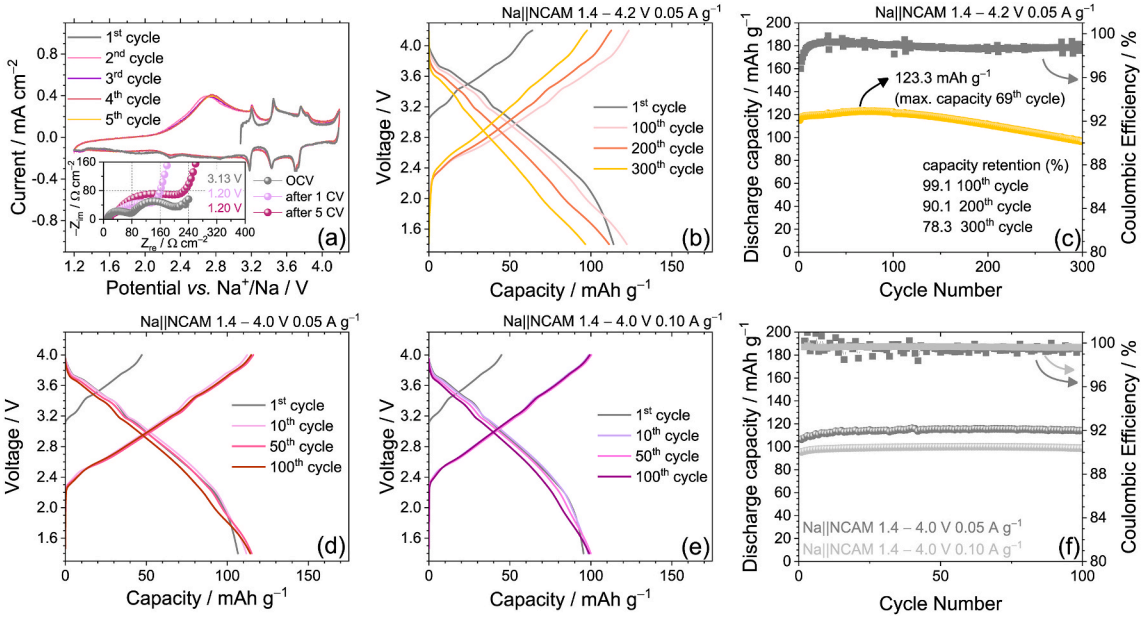

Fig. 5. Electrochemical response of the Na||NCAM half-cells, in detail: **(a)** CV profiles recorded between 1.2 and 4.2 V *vs.* Na^+/Na, inset shows Nyquist plot recorded by EIS during CV (test carried out at 25 °C); **(b, c)** selected voltage profiles **(b)** and discharge capacity trend **(c)**, with coulombic efficiency reported in right *y*-axis, related to galvanostatic cycling tests performed between 1.4 and 4.2 V at a specific current of 0.05 A g^{-1}; **(d, e, f)** selected voltage profiles related to galvanostatic cycling tests performed between 1.4 and 4.0 V at a current of **(d)** 0.05 A g^{-1} and **(e)** 0.10 A g^{-1} and **(f)** related discharge capacity trend (coulombic efficiency reported in right *y*-axis). Active material loading: 4.8–6.0 mg cm^{-2}, CV scan rate: 0.1 mV s^{-1}; EIS performed at the OCV cell condition and upon CV after the 1st and 5th cycle between 500 kHz and 100 mHz, alternate voltage signal with an amplitude of 10 mV. The galvanostatic tests were performed at 30 °C.

Table 2
NLLS analysis carried out on the Nyquist plots displayed as inset in Fig. 5a recorded on a three-electrode Na||NCAM half-cell at the OCV and after 1 and 5 CV runs.

Cell condition	Circuit	R_1 [Ω]	R_2 [Ω]	$R_I = \sum R_n$ [Ω]	χ^2
OCV	$R_e(R_1Q_1)(R_2Q_2)Q_w$	47.4 ± 1.1	103.6 ± 13.1	151.0 ± 13.1	4×10^{-4}
After 1 CV	$R_e(R_1Q_1)(R_2Q_2)Q_w$	21.5 ± 2.9	90.5 ± 8.3	112.0 ± 8.8	3×10^{-4}
After 5 CV	$R_e(R_1Q_1)(R_2Q_2)Q_w$	14.4 ± 2.1	152.2 ± 7.5	166.6 ± 7.8	4×10^{-4}

by the partial electrolyte oxidation or minor phase change at 4.2 V *vs.* Na^+/Na as discussed during CV [41]. The latter irreversible processes may be strongly limited by decreasing the charge voltage cutoff or by increasing the employed current, as demonstrated by the galvanostatic cycling tests performed on Na||NCAM cells hereafter. Initially, the galvanostatic performance of the Na||NCAM half-cell is investigated in the 1.4–4.2 V voltage range at 0.05 A g^{-1}, as reported in Fig. 5b in terms of voltage profiles and in Fig. 5c in terms of discharge capacity *vs.* cycle number trend. In line with the CV, the voltage profiles show an initial short charge (gray line) evolving through the series of plateaus described above from 3.2 to 4.1 V, and the side plateau at 4.2 V at the end of the charge possibly due to the partially irreversible processes. The initial charge with a capacity of about 60 mAh g^{-1} is reflected during the first discharge into multi-step process with an overall capacity of 115 mAh g^{-1}, accounting for the Na-deficiency of the NCAM, while the subsequent charge and discharge proceed reversibly with a slight increase of capacity upon cycling to 123 mAh g^{-1} at the 69th cycle, and a Coulombic efficiency approaching 99 % (see corresponding cycling trend in Fig. 5c). The latter capacity value is indeed selected to achieve the discharge capacity retention, which resulted in 78 % after 300 cycles. The excellent performance of the NCAM in the glyme-based solution within the experimental setup adopted herein represents a step forward compared to the one previously achieved by NCAM in carbonate-based one, where a higher capacity achieved by increasing the voltage cutoff was retained for only 60 % over 100 cycles due to the formation of insulating side products at the electrode/electrolyte interphase [41]. As mentioned above, a further improvement of the capacity retention may be achieved by lowering the charge cutoff to 4.0 V or by increasing the current, although a lower capacity may be expectedly achieved due to the limited exploitation of the NCAM electrochemical process. Accordingly, further galvanostatic tests are performed by limiting the voltage range to 1.4–4.0 V and using specific currents of either 0.05 or 0.1 A g^{-1} (Fig. 5d–f). The voltage profiles of the cells show similar features to those discussed previously in Fig. 5b without relevant signs of electrolyte decomposition, however with a lower capacity due to the lower voltage cutoff and/or higher current. Indeed, the cell cycled at 0.05 A g^{-1} (Fig. 5d) shows an initial charge capacity of ~50 mAh g^{-1} and a discharge one of ~115 mAh g^{-1}, while the one cycled at the higher current of 0.1 A g^{-1} (Fig. 5e) evidences a similar initial charge capacity and a reversible one of 96 mAh g^{-1}. Both cells proceed without any capacity fade over 100 cycles, with an average Coulombic efficiency ranging between 99.5 % and 99.6 % (see the capacity and efficiency trends in Fig. 5f), thus suggesting essentially the absence of irreversible reactions. To further understand the above discussed cell behavior, Fig. S2 (Supporting Information) shows the electrochemical stability toward oxidation of the DEGDME 1 M $NaPF_6$ electrolyte and the galvanostatic cycling coupled with EIS investigation of the NCAM cathode in Na half-cells. The electrolyte anodic stability is determined by LSV using a Na||SPC 3-electrode T-cell, the profile of which in Fig. S2a indicates current below 15 μA cm^{-2} from the cell OCV to 4.2 V *vs.* Na^+/Na, increasing to 28 μA cm^{-2} around 4.4 V *vs.* Na^+/Na, and then rapidly raising to high values due to electrolyte decomposition.

The effects of the upper voltage limit on cathode stability and interphase characteristics are investigated by galvanostatic cycling of Na||NCAM half-cells at 0.05 A g^{-1} with charge either up to 3.9, 4.0, 4.1, or 4.2 V, carrying out the EIS after the 1st, 5th, 10th, and 50th discharge. The related cycling trends summarized in Fig. S2b evidence a capacity retention always exceeding 93 %, with modest influence of the voltage cutoff, despite the cell charged up to 4.2 V displays the lowest retention as expected by more relevant electrolyte decomposition. The EIS Nyquist plots for the cells at the OCV and upon cycling are collected in Fig. S2c–d, and the overall interphase resistance (R_I) is achieved by NLLS analysis in Table S1 as sum of the resistance values defined by each semicircle in the corresponding equivalent circuit. The trends of R_I reported in Fig. S3 reveal for the cells cycled in the 1.4–3.9 V and 1.4–4.0 V intervals a resistance decrease upon first cycle, due to partial dissolution of the SEI, and an increase after the subsequent cycles due to its thickening and stabilization upon partial electrolyte decomposition [41,43,64]. On the other hand, the cell cycled in the 1.4–4.1 V interval shows resistance increase after 1 cycle, decrease after 5 cycles, and final raise until the end of the test, thus suggesting initial growth, subsequent partial dissolution, and final thickening of the SEI. Instead, the cell cycled in the 1.4–4.2 V interval depicts a continuous resistance increase upon cycling, thus accounting for permanent thickening of the SEI within the wider voltage window, as also suggested by the lowest retention already shown in Fig. S2. On the other hand, the high efficiency of the NCAM cathodes and the excellent performances of the $(Na_xSn\text{-}C)_{27min}$ anodes within the operating voltage and current conditions indicate their combination in a glyme-based electrolyte as potentially suitabile for achieving balanced Na-ion full-cells.

3.3. Full Na-ion battery

Recently, only few reports have studied SIBs exploiting Na-deficient cathodes and alloying anodes, mainly due to the challenges associated with these active materials [31,86]. Herein, we concomitantly overcome the Na-deficiency of the NCAM and the initial irreversibility of the Sn-C by rationally balancing the sodium content into a $(Na_xSn\text{-}C)_{27min}$ electrode, to ensure an N/P ratio between 1.1 and 1.3. In addition, we use electrodes with relatively high active material loading, as shown by the anode and cathode voltage profile delivered upon the first cycle in the example of Fig. S4 (Supporting Information). Accordingly, Fig. 6 reports the results related to galvanostatic cycling of full $(Na_xSn\text{-}C)_{27min}$||NCAM cells (see representative scheme in Fig. 6a) under various conditions, as well as to the *ex situ* XRD analysis carried out on the electrodes after cycling. In line with the outcomes of anode and cathode above observed in the half-cells investigations, a first test is carried out by cycling the full-cells in the 0.8–4.2 V voltage range either at 0.05 A g^{-1} or at 0.1 A g^{-1} as displayed in Fig. 6b and c, respectively, and in terms of selected voltage profiles, and in Fig. 6d in terms of comparison of discharge capacity *vs.* cycle number trends. The full-cells reveal both at 0.05 A g^{-1} (Fig. 6b) and at 0.1 A g^{-1} (Fig. 6c) a sloped voltage shape, resulting from the combination of the anode and cathode ones, with maximum discharge capacity respectively of 115 mAh g^{-1} and 110 mAh g^{-1}, retained for ~85 % over 100 cycles with average Coulombic efficiency exceeding 99 % (Fig. 5d). This stable behavior indicates an optimal cell balance, with only slight influence of the applied current. It is worth mentioning that literature works suggested further improvement of the cell performance by adopting *ad hoc* designed formation cycles [87,88]. To further promote the stability, the full-cells are galvanostatically cycled in the restricted voltage ranges of 0.8–4.0 V and 0.8–3.9 V, using a current rate of 0.05 A g^{-1} as displayed in Fig. 6e and f in terms of voltage profiles and in Fig. 6g and h in terms of discharge capacity *vs.* cycle number trend. Lowering the charge cutoff does not significantly affect the cell capacity, which stabilizes around 115 mAh g^{-1} in both cases, as also promoted by the additional potentiostatic step adopted in the case of the cell charged at the lowest voltage cutoff (see experimental section for further details). The voltage profiles of Fig. 6e and f reveal slight increase of the charge/discharge polarization during cycling,

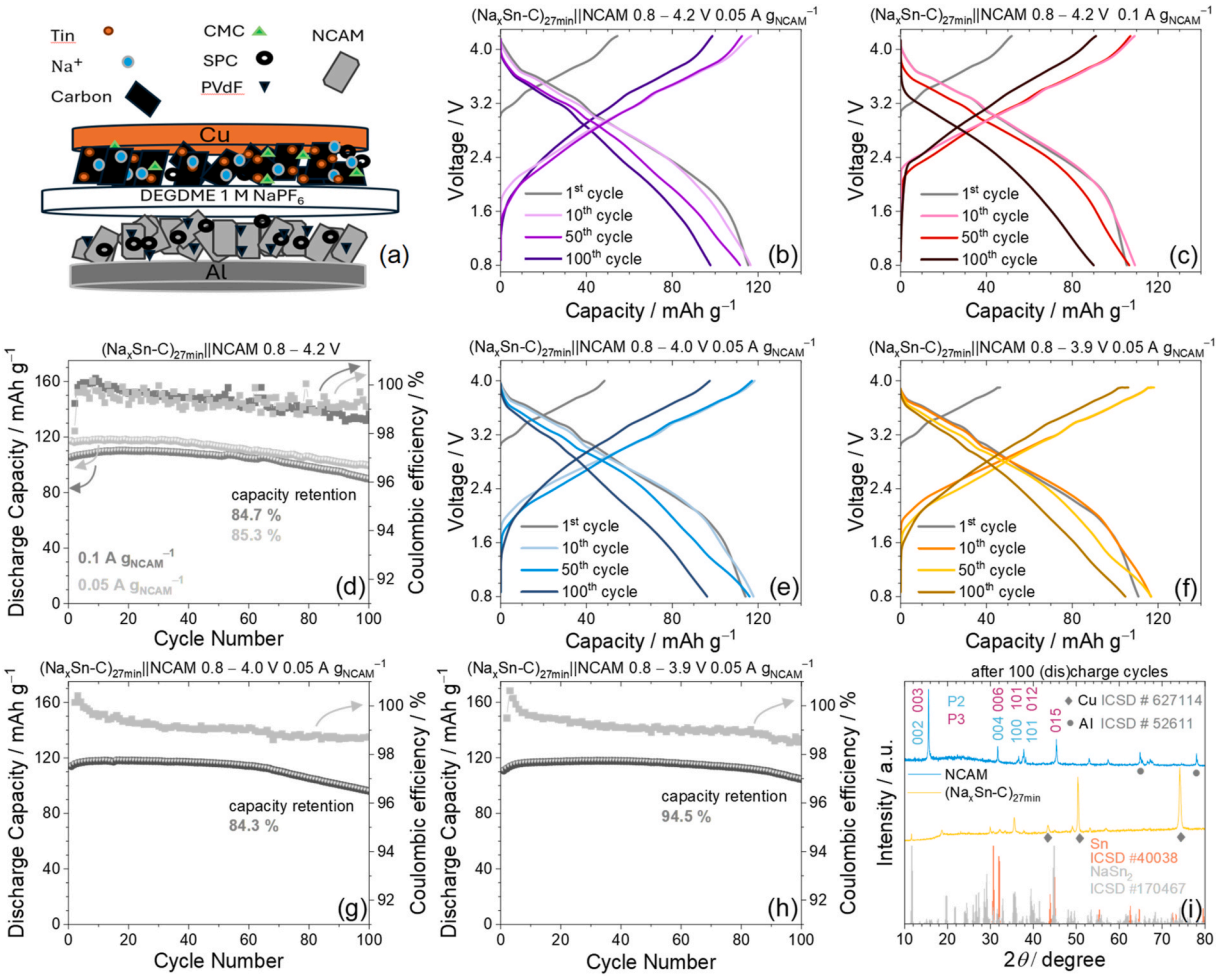

Fig. 6. **(a)** Schematic representation of the sodium-ion battery configuration; **(b–h)** galvanostatic cycling performance of $(Na_xSn\text{-}C)_{27min}$||NCAM full-cells at various conditions reported in the panels, in detail:, **(b, c, e, f)** selected voltage profiles and **(d, g, h)** corresponding discharge capacity *vs.* cycle number trends (Coulombic efficiency in right-hand side *y*-axes); **(i)** *ex situ* X-ray diffractograms of $(Na_xSn\text{-}C)_{27min}$ and NCAM electrodes after 100 cycles between 0.8 and 4.0 V. Electrode geometric area: 1.54 cm^2; active material loading: 5.3–6.8 mg_{NCAM} cm^{-2}, 3.5–4.5 $mg_{Sn\text{-}C}$ cm^{-2}; N/P ratio between 1.1 and 1.2. Temperature for galvanostatic cycling: 30 °C.

although the typical voltage shape of NCAM remains almost unaltered, thus suggesting the retention of the corresponding electrochemical activity. Relevantly, the cell cycled using 4.0 V as the charge cutoff retains about 85 % of the initial maximum capacity upon 100 (dis)charge runs, similarly to that charged up to 4.2 V, while the one exploiting the 3.9 V cutoff retains 95 % over the same cycling interval. This retention improvement may be ascribed to the high and stable efficiency in view of a mitigated electrolyte decomposition at the cathode side, as already discussed in the half-cells study in Fig. 5f, although a still observed capacity decrease occurring upon cycling indicates the need for further optimizations both in terms of cycling conditions and electrolyte composition. The structural features of NCAM and $(Na_xSn\text{-}C)_{27min}$ upon 100 cycles are investigated by *ex-situ* XRD on the full-cell cycled between 0.8 and 4.0 V of Fig. 6e,g and the acquired patterns are reported in Fig. 6i. The figure evidences the structural retention for the NCAM cathode, as all the main peaks of the mixed P2/P3 layered oxide hold their position after cycling, due to the enhanced stability toward phase transition favored by the presence of Al^{3+} [41]. Instead, the $(Na_xSn\text{-}C)_{27min}$ structure after galvanostatic cycling appears different compared to the spectra of the pristine Sn-C reported in Fig. 1b. Indeed, the XRD pattern in Fig. 6i shows less intense peaks for elemental Sn and signals related to the $NaSn_2$ phase at 12° and 36°, thus indicating only partial dealloying upon full-cell discharge. This outcome suggests incomplete anode exploitation potentially affecting the capacity retention in the full-cell, which can be addressed by further tuning the N/P ratio and by improving the testing procedures.

With the aim of further investigating the $(Na_xSn\text{-}C)_{27min}$||NCAM cell in terms of energy content, Fig. 7 reports a rate capability test combined with EIS study, carried out in the intermediate 0.8–4.1 V voltage range by increasing the current every 5 cycles from 0.05 A g^{-1} to 0.10, 0.15, 0.20, and 0.25 A g^{-1} before lowering the current back to 0.05 A g^{-1} at the 26th cycle. The corresponding voltage profiles (Fig. 7a) depict the shape expected by the galvanostatic tests already discussed in Fig. 6, with moderate polarization upon current rate increase, and a maximum capacity of ~120 mAh g^{-1} achieved at the lowest current. Interestingly, the cell delivers about 90 % of its maximum capacity by doubling the current from 0.05 to 0.1 A g^{-1}, and still a relevant 78 % of the maximum value by five-fold current increase, from 0.05 to 0.25 A g^{-1}. Fig. 7b displays the theoretical energy density values for the Na-ion cell as referred either to the NCAM cathode mass (bottom x-axis) or to the overall active materials mass, namely NCAM and $(Na_xSn\text{-}C)_{27min}$ (top x-axis), estimated by taking into account the corresponding voltage profiles at the 5th cycle at each current rate of Fig. 7a. The figure shows an energy density ranging from 250 Wh kg^{-1} to 310 Wh kg^{-1} as referred to the NCAM cathode mass, which turns into a value ranging from 115 Wh kg^{-1} to 170 Wh kg^{-1} when the overall anode plus cathode mass is taken into account. In addition to the normalization reported in Fig. 7b, Fig. S5 (Supporting Information) provides a parallel normalization of energy

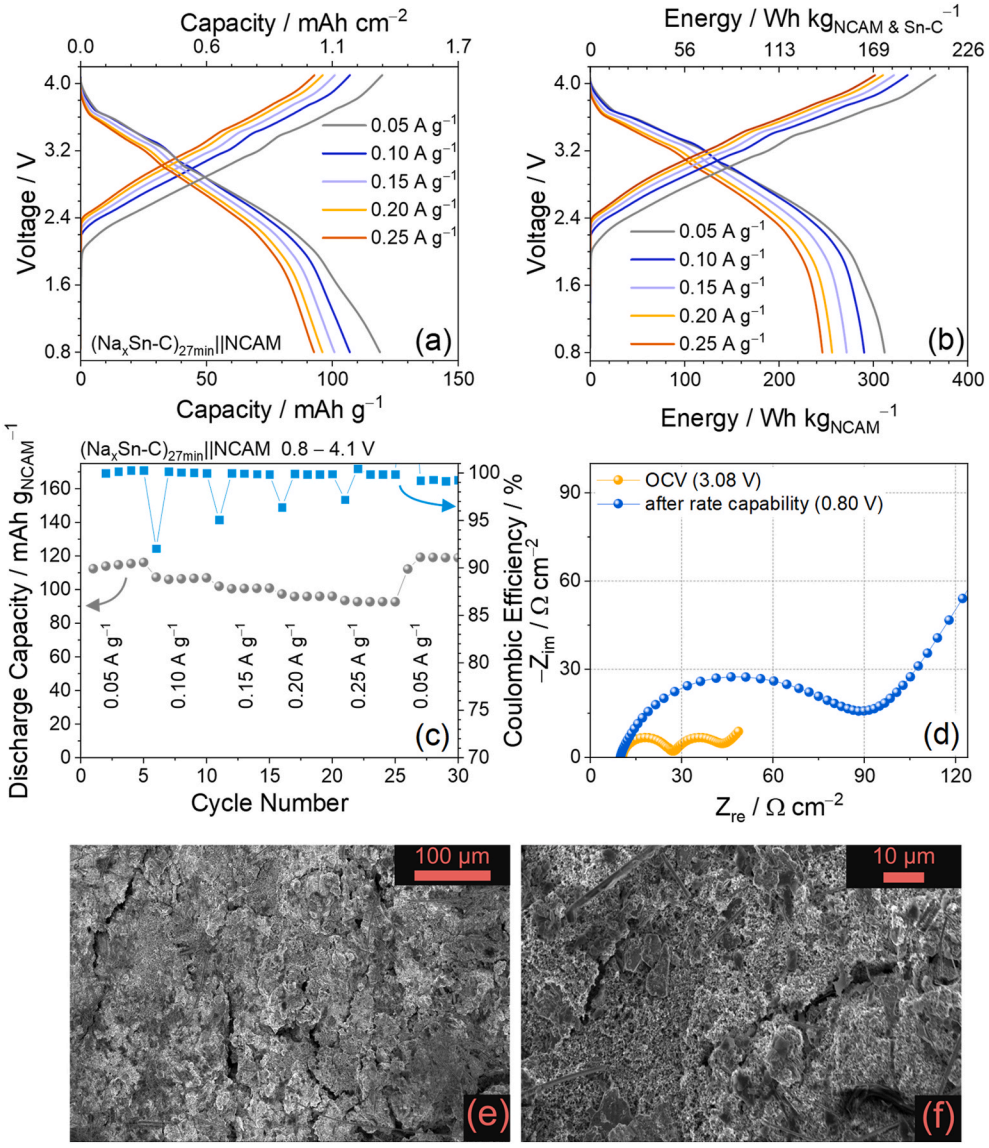

Fig. 7. Galvanostatic cycling performance upon current rate capability test of (Na$_x$Sn-C)$_{27min}$||NCAM full-cell, in detail: **(a)** selected voltage profiles (5th of each current rate explored), **(b)** corresponding representation of the charge/discharge voltage *vs.* energy density (top *x*-axis refers to both electrodes active material masses, while bottom *x*-axis refers to NCAM mass only), **(c)** capacity trend *vs.* cycle number (coulombic efficiency in right-hand side *y*-axis), **(d)** electrochemical characterization of the electrodes/electrolyte interphases through Nyquist plot recorded by EIS (data collected before cycling and after the 30th discharge), **(e, f)** SEM images at different magnification of the (Na$_x$Sn-C)$_{27min}$ electrode retrieved from cycled full-cell. Electrodes geometric area: 0.785 cm^2, active material: 11.5 ± 0.1 mg$_{NCAM}$ cm^{-2}, 7.6 ± 0.1 mg$_{Sn\text{-}C}$ cm^{-2}. Active material ratio: 1.28, N/P ratio: 1.1. Tests performed at 25 °C.

density taking into account the full electrodes including current collectors, binder, and electronic conductor (SPC), as well as their stack with separator/electrolyte, for enabling possible benchmarking. Hence, the cell delivers over 90 Wh kg^{-1} when full electrodes are considered, and 60 Wh kg^{-1} when the stack with separator (Whatman GF/B)/electrolyte is considered, which are lower values than the theoretical ones, clearly reflecting the laboratory-scale nature of the cell. It is worth mentioning that these values may be actually increased by scaling-up the cell to limit the mass contribution of elements such as current collectors, separators and electrolytes. For example, changing the separator from Whatman GF/B to celgard, which can allow a lower electrolyte/electrode mass ratio of 1–2 μL/mg, increases the energy density referred to the stack with separator/electrolyte from 60 Wh kg^{-1} to 80 Wh kg^{-1}. On the other hand, the cell shows a Coulombic efficiency exceeding 99 % after the first cycle at each current, and a full capacity retention by lowering back the current to the initial value after the rate capability test (see corresponding trend in Fig. 7c). The interphase modifications of the electrodes by full-cell cycling are investigated by the EIS Nyquist plots in Fig. 7d, and NLLS analysis using the resistive and pseudocapacitive elements in the equivalent circuit of Table 3. The elements account for electrolyte resistance, and the combined Na^+ diffusion and transfer events in the two electrodes. The (Na$_x$Sn-C)$_{27min}$||NCAM cell exhibits

Table 3
NLLS analysis carried out on the Nyquist plots displayed in Fig. 7d. The impedance spectra were acquired on the (Na$_x$Sn-C)$_{27min}$||NCAM cell at the OCV and after the current rate capability test, and fitted using the Boukamp software, by exclusively accepting results with χ^2 values of the order of 10^{-4} or lower.

Cell condition	Circuit	R_1 [Ω]	R_2 [Ω]	$R_I = \sum R_n$ [Ω]	χ^2
OCV	$R_e(R_1Q_1)(R_2Q_2)Q_w$	12.5 ± 0.1	14.1 ± 1.0	26.6 ± 1.0	3×10^{-4}
After 30 cycles	$R_e(R_1Q_1)\ Q_w$	59.5 ± 1.2	/	59.5 ± 1.2	3×10^{-4}

EIS responses characterized by relatively low interphase resistance at the OCV, settling at 27 Ω and moderately increasing upon stabilization of the interphase at 60 Ω, that is, a modest value accounting for the cell stability and relevant capacity retention driven by the adequate setup in terms of electrodes features. The electrochemical process retention is further demonstrated by the CV response of the $(Na_xSn\text{-}C)_{27min}$||NCAM full-cell reported in Fig. S6 (Supporting Information), carried out after the current rate capability test of Fig. 7. The CV clearly shows the combined electrochemical features of the anode and cathode materials, evolving with a still distinguishable detail. Beside the stability of the cathode above demonstrated, a further interesting proof of the integrity of the water-processed anode using the CMC binder is given by the SEM images of the $(Na_xSn\text{-}C)_{27min}$ anode retrieved from the full-cell upon cycling. The images reported in Fig. 7e and f with different magnifications depict a uniform morphology, characterized by a rough surface reasonably due to the CMC, wrapping-up the micrometric Sn-C particles, some of which are clearly visible at higher magnification (Fig. 7f). Moreover, the low amount of cracks spotted onto the surface may suggest limited changes through the electrode caused by the volume variation upon cycling.

The lifetime/energy trade-off in the 1.4–3.9/4.0/4.1/4.2 V voltage ranges is gathered by analyzing the Na||NCAM half-cells of Fig. S2 and the $(Na_xSn\text{-}C)_{27min}$||NCAM full cells of Fig. 6 in term of trends of the *discharge mean voltage* upon cycling, as reported in Fig. S7. The comparison of the above trends in half-cells (Fig. S7a) and full-cells (Fig. 7b) shows that the more conservative testing condition (*i.e.*, charge to 3.9 V at 0.05 A g^{-1}) lowers down the discharge mean voltage due to incomplete charge, while enhances the retention of the same parameter as the side reactions on NCAM are mitigated compared to the more demanding condition (*i.e.*, charge to 4.2 V at 0.05 A g^{-1}). On the other hand, the full-cell charged up to 4.2 V at the higher current of 0.10 A g^{-1} (Fig. 4b) retains its mean voltage more than those cycled at 0.05 A g^{-1} since the side reactions are mitigated, thus indicating that the applied current plays a key role for full-cell stability. To further verify this aspect, two Na||NCAM half-cells are galvanostatically cycled between 1.2 and 4.4 V by applying a current of either 0.05 A g^{-1} or 0.12 A g^{-1}. The related results presented in Fig. S7c and d in terms of selected voltage profiles and discharge capacity trends clearly show that the voltage shape is less retained at lower current than higher one, due to more pronounced electrolyte decomposition. However, we do not exclude possible side reactions due to NCAM irreversible structural changes at high voltage.

4. Conclusion

In this work we provided a viable pathway to achieve highly cyclable Na-ion full-cells based on layered-oxide cathode, Na-alloying anode water-processed with CMC binder, and a glyme-based electrolyte. The P3/P2 NCAM cathode showed relevant stability and efficiency in Na-half cell, maximum discharge capacity of 161.1 mAh g^{-1}, as well as a modest interphase resistance and structural stability, despite it appeared quite challenging for full-cell implementation due to its native sodium-deficiency. The NCAM interphase proprieties depended on the adopted upper voltage limit (*i.e.*, 3.9, 4.0, 4.1, or 4.2 V), thus suggesting the implementation of suitable protocols for enhancing the cell efficiency during galvanostatic cycling. On the other hand, the Na-alloying Sn-C anode outperformed the hard-carbons in Na-cell reported in literature due to a high volumetric capacity, relevant stability, and suitable interphase features. However, the relevant irreversibility during the first cycle hampered its direct application at the pristine state in a balanced and efficient Na-ion full-cell. We have concomitantly overcome the above two issues (*i.e.*, Na-deficiency in NCAM and Sn-C first cycle irreversibility) by adopting an alternative approach, consisting of chemical pre-sodiation of the alloying anode prior to the use in Na-ion full-cell. This process actually allowed the anode to act as the Na reservoir in an efficient full-cell using the NCAM cathode, by tuning the electrode loading, the binder nature, the electrolyte formulation, and the Na/Sn-C contacting timeframe. Galvanostatic and potentiostatic techniques assessed the electrochemical suitability of the $(Na_xSn\text{-}C)_{27min}$ anode for full-cell application, while SEM-EDS analysis depicted a uniform morphology having evenly-distributed Na across the electrode pre-treated following our protocol. The full-cells, achieved by rationally combining a Sn-C anode pre-sodiated for 27 min and the NCAM cathode with a N/P ratio from 1.1 to 1.2, revealed high cycling stability, with maximum capacity around 120 mAh g^{-1}, that approached the maximum electrodes capacity achieved in half-cell. Furthermore, the full-cell performance has been retained between 85 % and 95 % of the maximum capacity over 100 galvanostatic (dis)charge cycles, depending on experimental constraints such as voltage cutoff from 3.9 to 4.1 V, and applied current from 0.05 to 0.25 A g^{-1}. This optimal retention has been supported by XRD, CV and ex-situ SEM images. Hence, we have estimated for our $(Na_xSn\text{-}C)_{27min}$||NCAM full-cell an energy density ranging from 310 to 250 Wh kg^{-1}, based on the cathode mass only, which reflected values from 175 to 141 Wh kg^{-1} considering both electrodes active material, whilst lower values considering all the cell components, including inactive ones, that may be further improved by tuning the materials for possible cell scaling-up. These results suggested our approach as suitable for achieving an enhanced Na-ion battery, despite further improvements in terms of cycle life and stability may be achieved by additional optimization of the electrodes balancing, cell operation conditions, and electrolyte.

CRediT authorship contribution statement

Edoardo Barcaro: Writing – original draft, Visualization, Methodology, Investigation, Formal analysis, Data curation, Conceptualization. **Daniel Amato:** Visualization, Methodology, Investigation. **Vittorio Marangon:** Writing – review & editing, Visualization, Methodology, Investigation, Data curation. **Dominic Bresser:** Writing – review & editing, Visualization, Supervision, Resources. **Jusef Hassoun:** Writing – review & editing, Writing – original draft, Visualization, Supervision, Project administration, Methodology, Funding acquisition, Formal analysis, Data curation, Conceptualization.

Declaration of competing interest

The authors declare that they have no known competing financial interests or personal relationships that could have appeared to influence the work reported in this paper.

Acknowledgements

Project funded under the National Recovery and Resilience Plan (NRRP), Mission 04 Component 2 Investment 1.5 – NextGenerationEU, Call for tender n. 3277 dated 30/12/2021, Award Number: 0001052 dated 23/06/2022. The authors also thank the grant “Fondo di Ateneo per la Ricerca Scientifica, FAR 2024” University of Ferrara, and the project “Accordo di Collaborazione Quadro 2015” between University of Ferrara, Italy (Department of Chemical and Pharmaceutical Sciences) and Sapienza University of Rome, Italy (Department of Chemistry).

Appendix A. Supplementary data

Supplementary data to this article can be found online at https://doi.org/10.1016/j.jpowsour.2025.239124.

Data availability

Data will be made available on request.

References

[1] B. Scrosati, Lithium rocking chair batteries: an old concept? J. Electrochem. Soc. 139 (1992) 2776–2781, https://doi.org/10.1149/1.2068978.

[2] I. Hasa, S. Mariyappan, D. Saurel, P. Adelhelm, A.Y. Koposov, C. Masquelier, L. Croguennec, M. Casas-Cabanas, Challenges of today for Na-based batteries of the future: from materials to cell metrics, J. Power Sources 482 (2021) 228872, https://doi.org/10.1016/j.jpowsour.2020.228872.

[3] J.-M. Tarascon, Na-ion versus Li-ion batteries: complementarity rather than competitiveness, Joule 4 (2020) 1616–1620, https://doi.org/10.1016/j.joule.2020.06.003.

[4] F. Duffner, N. Kronemeyer, J. Tübke, J. Leker, M. Winter, R. Schmuch, Post-lithium-ion battery cell production and its compatibility with lithium-ion cell production infrastructure, Nat. Energy 6 (2021) 123–134, https://doi.org/10.1038/s41560-020-00748-8.

[5] C. Vaalma, D. Buchholz, M. Weil, S. Passerini, A cost and resource analysis of sodium-ion batteries, Nat. Rev. Mater. 3 (2018) 18013, https://doi.org/10.1038/natrevmats.2018.13.

[6] V. Marangon, K. Bischof, A.A. Regalado, M. Keppeler, M. Pogosova, M. Wan, J. Choi, S. Fleischmann, T. Diemant, M. Wohlfahrt-Mehrens, M. Hölzle, T. Waldmann, D. Bresser, Cell design and chemistry of commercial sodium-ion battery cells, J. Power Sources 634 (2025) 236496, https://doi.org/10.1016/j.jpowsour.2025.236496.

[7] A. Yao, S.M. Benson, W.C. Chueh, Critically assessing sodium-ion technology roadmaps and scenarios for techno-economic competitiveness against lithium-ion batteries, Nat. Energy 10 (2025) 404–416, https://doi.org/10.1038/s41560-024-01701-9.

[8] J.W. Choi, D. Aurbach, Promise and reality of post-lithium-ion batteries with high energy densities, Nat. Rev. Mater. 1 (2016) 16013, https://doi.org/10.1038/natrevmats.2016.13.

[9] K. Bischof, V. Marangon, M. Kasper, A. Aracil Regalado, M. Wohlfahrt-Mehrens, M. Hölzle, D. Bresser, T. Waldmann, Evaluation of commercial 18650 and 26700 sodium-ion cells and comparison with well-established lithium-ion cells, Journal of Power Sources Advances 27 (2024) 100148, https://doi.org/10.1016/j.powera.2024.100148.

[10] X. Liang, J. Hwang, Y. Sun, Practical cathodes for sodium-ion batteries: who will take The Crown? Adv. Energy Mater. 13 (2023) 2301975 https://doi.org/10.1002/aenm.202301975.

[11] Q. Liu, Z. Hu, M. Chen, C. Zou, H. Jin, S. Wang, S. Chou, Y. Liu, S. Dou, The cathode choice for commercialization of sodium-ion batteries: layered transition metal oxides versus prussian blue analogs, Adv. Funct. Mater. 30 (2020) 1909530, https://doi.org/10.1002/adfm.201909530.

[12] F. Cheng, J. Hu, W. Zhang, B. Guo, P. Yu, X. Sun, J. Peng, Reviving ether-based electrolytes for sodium-ion batteries, Energy Environ. Sci. (2025) 6874–6898, https://doi.org/10.1039/D5EE00725A.

[13] Z. Song, Z. Xing, J. Yang, J. Chen, W. Hu, P. Li, W. Feng, G.G. Eshetu, E. Figgemeier, S. Passerini, M. Armand, Z. Zhou, H. Zhang, Electrolyte chemistry development for sodium-based batteries: a blueprint from lithium or a step toward originality? Angew. Chem. Int. Ed. 64 (2025) e202424543 https://doi.org/10.1002/anie.202424543.

[14] Y. Li, F. Wu, Y. Li, M. Liu, X. Feng, Y. Bai, C. Wu, Ether-based electrolytes for sodium ion batteries, Chem. Soc. Rev. 51 (2022) 4484–4536, https://doi.org/10.1039/D1CS00948F.

[15] Z. Tian, Y. Zou, G. Liu, Y. Wang, J. Yin, J. Ming, H.N. Alshareef, Electrolyte solvation structure design for sodium ion batteries, Adv. Sci. 9 (2022) 2201207, https://doi.org/10.1002/advs.202201207.

[16] H. Darjazi, M. Falco, F. Colò, L. Balducci, G. Piana, F. Bella, G. Meligrana, F. Nobili, G.A. Elia, C. Gerbaldi, Electrolytes for sodium ion batteries: the Current transition from liquid to solid and hybrid systems, Adv. Mater. 36 (2024) 2313572, https://doi.org/10.1002/adma.202313572.

[17] H. Moriwake, A. Kuwabara, C.A.J. Fisher, Y. Ikuhara, Why is sodium-intercalated graphite unstable? RSC Adv. 7 (2017) 36550–36554, https://doi.org/10.1039/C7RA06777A.

[18] M. Dahbi, N. Yabuuchi, K. Kubota, K. Tokiwa, S. Komaba, Negative electrodes for Na-ion batteries, Phys. Chem. Chem. Phys. 16 (2014) 15007, https://doi.org/10.1039/c4cp00826j.

[19] H. Kim, J. Hong, G. Yoon, H. Kim, K.-Y. Park, M.-S. Park, W.-S. Yoon, K. Kang, Sodium intercalation chemistry in graphite, Energy Environ. Sci. 8 (2015) 2963–2969, https://doi.org/10.1039/C5EE02051D.

[20] X. Dou, I. Hasa, D. Saurel, C. Vaalma, L. Wu, D. Buchholz, D. Bresser, S. Komaba, S. Passerini, Hard carbons for sodium-ion batteries: structure, analysis, sustainability, and electrochemistry, Mater. Today 23 (2019) 87–104, https://doi.org/10.1016/j.mattod.2018.12.040.

[21] C. Albenga, J.A. Gott, A. Skurtveit, J.M. Warnett, F.M. Maddar, A.Y. Koposov, G. Pinzón, G. West, I. Hasa, Assessing the role of morphological changes as the origin of improved cycling stability of Sn-based anodes for sodium-ion batteries, J Mater Chem A 13 (2025) 30967–30984, https://doi.org/10.1039/D5TA03000E.

[22] M.D.L. Garayt, M.C. Obialor, I.L. Monchesky, A.E. George, S. Yu, B.A. Rutherford, M. Metzger, J.R. Dahn, Restructuring of sodium-lead alloys during charge-discharge cycling in sodium-ion batteries, J. Electrochem. Soc. 171 (2024) 120521, https://doi.org/10.1149/1945-7111/ad9bf0.

[23] C. Kim, H. Kim, M.K. Sadan, M. Jeon, G.-B. Cho, T.-H. Nam, K.-K. Cho, J.-H. Ahn, H.-J. Ahn, A high rate and long-cycle-life anode based on micrometer-sized Pb powder for sodium-ion batteries, J. Alloys Compd. 886 (2021) 161240, https://doi.org/10.1016/j.jallcom.2021.161240.

[24] N. Yabuuchi, Y. Matsuura, T. Ishikawa, S. Kuze, J. Son, Y. Cui, H. Oji, S. Komaba, Phosphorus Electrodes in sodium cells: small volume expansion by sodiation and the surface-stabilization mechanism in aprotic solvent, Chemelectrochem 1 (2014) 580–589, https://doi.org/10.1002/celc.201300149.

[25] Y. Liu, Q. Liu, C. Jian, D. Cui, M. Chen, Z. Li, T. Li, T. Nilges, K. He, Z. Jia, C. Zhou, Red-phosphorus-impregnated carbon nanofibers for sodium-ion batteries and liquefaction of red phosphorus, Nat. Commun. 11 (2020) 2520, https://doi.org/10.1038/s41467-020-16077-z.

[26] S.-M. Oh, P. Oh, S.-O. Kim, A. Manthiram, A high-performance sodium-ion full cell with a layered oxide cathode and a phosphorous-based composite anode, J. Electrochem. Soc. 164 (2017) A321–A326, https://doi.org/10.1149/2.0931702jes.

[27] A. Skurtveit, A. Pastusic, A. Brennhagen, F.M. Maddar, C.E. Mohn, A. Karmakar, C. A. O'Keefe, I. Hasa, C. Cavallo, B. Arstad, H. Fjellvåg, D.S. Wragg, A.Y. Koposov, Unique $Na_{5-x}SbSe$ phase enables high-rate performance of Sb_2Se_3 anodes in Na-Ion batteries, Adv. Energy Mater. 15 (2025) 2501433, https://doi.org/10.1002/aenm.202501433.

[28] L. Baggetto, H.-Y. Hah, C.E. Johnson, C.A. Bridges, J.A. Johnson, G.M. Veith, The reaction mechanism of FeSb2 as anode for sodium-ion batteries, Phys. Chem. Chem. Phys. 16 (2014) 9538, https://doi.org/10.1039/c4cp00738g.

[29] Y. Kravets, Y. Sun, H. Wang, P. Adelhelm, Role of silicon as structural stabilizer and redox-active element in multicomponent (Sn, Sb, Fe, Si) alloy electrodes for Na-ion batteries, Batter Supercaps 8 (2025) e202400690, https://doi.org/10.1002/batt.202400690.

[30] B. Zhang, G. Rousse, D. Foix, R. Dugas, D.A.D. Corte, J. Tarascon, Microsized Sn as advanced anodes in glyme-based electrolyte for Na-Ion batteries, Adv. Mater. 28 (2016) 9824–9830, https://doi.org/10.1002/adma.201603212.

[31] T. Perveen, M. Siddiq, N. Shahzad, R. Ihsan, A. Ahmad, M.I. Shahzad, Prospects in anode materials for sodium ion batteries - a review, Renew. Sustain. Energy Rev. 119 (2020) 109549, https://doi.org/10.1016/j.rser.2019.109549.

[32] H. Tan, D. Chen, X. Rui, Y. Yu, Peering into alloy anodes for sodium-ion batteries: current trends, challenges, and opportunities, Adv. Funct. Mater. 29 (2019) 1808745, https://doi.org/10.1002/adfm.201808745.

[33] L.D. Ellis, T.D. Hatchard, M.N. Obrovac, Reversible insertion of sodium in tin, J. Electrochem. Soc. 159 (2012) A1801–A1805, https://doi.org/10.1149/2.037211jes.

[34] L.Y. Beaulieu, K.W. Eberman, R.L. Turner, L.J. Krause, J.R. Dahn, Colossal reversible volume changes in lithium alloys, Electrochem. Solid State Lett. 4 (2001) A137–A140, https://doi.org/10.1149/1.1388178.

[35] M.D.L. Garayt, L. Zhang, Y. Zhang, M.C. Obialor, J. Deshmukh, Y. Xing, C. Yang, M. Metzger, J.R. Dahn, Practical alloy-based negative electrodes for Na-ion batteries, J. Electrochem. Soc. 171 (2024) 070523, https://doi.org/10.1149/1945-7111/ad5e64.

[36] S. Komaba, Y. Matsuura, T. Ishikawa, N. Yabuuchi, W. Murata, S. Kuze, Redox reaction of Sn-polyacrylate electrodes in aprotic Na cell, Electrochem. Commun. 21 (2012) 65–68, https://doi.org/10.1016/j.elecom.2012.05.017.

[37] X. Wu, X. Lan, R. Hu, Y. Yao, Y. Yu, M. Zhu, Tin-Based anode materials for stable sodium storage: progress and perspective, Adv. Mater. 34 (2022) 2106895, https://doi.org/10.1002/adma.202106895.

[38] D. Bresser, D. Buchholz, A. Moretti, A. Varzi, S. Passerini, Alternative binders for sustainable electrochemical energy storage – the transition to aqueous electrode processing and bio-derived polymers, Energy Environ. Sci. 11 (2018) 3096–3127, https://doi.org/10.1039/C8EE00640G.

[39] A. Beda, F. Rabuel, M. Morcrette, S. Knopf, P.-L. Taberna, P. Simon, C. Matei Ghimbeu, Hard carbon key properties allow for the achievement of high Coulombic efficiency and high volumetric capacity in Na-ion batteries, J Mater Chem A Mater 9 (2021) 1743–1758, https://doi.org/10.1039/D0TA07687B.

[40] Y. Yang, Z. Liu, Q. Zhang, J. Song, W. Li, S. Jiang, C. Zhang, J. Han, H. Yang, X. Han, S. He, Recent advances of high-rate hard carbon anodes for sodium-ion batteries: correlations between performance and microstructure, Adv. Funct. Mater. (2025) e14132, https://doi.org/10.1002/adfm.202514132.

[41] D. Di Lecce, V. Marangon, M. Isaacs, R. Palgrave, P.R. Shearing, J. Hassoun, Degradation of layered oxide cathode in a sodium battery: a detailed investigation by X-Ray Tomography at the nanoscale, Small Methods 5 (2021) 2100596, https://doi.org/10.1002/smtd.202100596.

[42] D. Di Lecce, D. Campanella, J. Hassoun, Insight on the enhanced reversibility of a multimetal layered oxide for sodium-ion battery, J. Phys. Chem. C 122 (2018) 23925–23933, https://doi.org/10.1021/acs.jpcc.8b07596.

[43] I. Hasa, S. Passerini, J. Hassoun, Toward high energy density cathode materials for sodium-ion batteries: investigating the beneficial effect of aluminum doping on the P2-type structure, J Mater Chem A Mater 5 (2017) 4467–4477, https://doi.org/10.1039/C6TA08667E.

[44] X. Liang, X. Song, H.H. Sun, H. Kim, M.-C. Kim, Y.-K. Sun, High-energy and long-life O3-type layered cathode material for sodium-ion batteries, Nat. Commun. 16 (2025) 3505, https://doi.org/10.1038/s41467-025-58637-1.

[45] T.-Y. Yu, J. Kim, G. Oh, M.H. Alfaruqi, J.-Y. Hwang, Y.-K. Sun, High-voltage stability of O3-type sodium layered cathode enabled by preferred occupation of Na in the OP2 phase, Energy Storage Mater. 61 (2023) 102908, https://doi.org/10.1016/j.ensm.2023.102908.

[46] Y.-J. Guo, P.-F. Wang, Y.-B. Niu, X.-D. Zhang, Q. Li, X. Yu, M. Fan, W.-P. Chen, Y. Yu, X. Liu, Q. Meng, S. Xin, Y.-X. Yin, Y.-G. Guo, Boron-doped sodium layered oxide for reversible oxygen redox reaction in Na-ion battery cathodes, Nat. Commun. 12 (2021) 5267, https://doi.org/10.1038/s41467-021-25610-7.

[47] X. Yuan, Y. Guo, L. Gan, X. Yang, W. He, X. Zhang, Y. Yin, S. Xin, H. Yao, Z. Huang, Y. Guo, A universal strategy toward air-stable and high-rate O3 layered oxide

cathodes for Na-Ion batteries, Adv. Funct. Mater. 32 (2022) 2111466, https://doi.org/10.1002/adfm.202111466.
[48] S.-M. Oh, S.-T. Myung, J.-Y. Hwang, B. Scrosati, K. Amine, Y.-K. Sun, High capacity O3-Type Na[$Li_{0.05}(Ni_{0.25}Fe_{0.25}Mn_{0.5})_{0.95}$]$O_2$ cathode for sodium ion batteries, Chem. Mater. 26 (2014) 6165–6171, https://doi.org/10.1021/cm502481b.
[49] S. Birgisson, T.L. Christiansen, B.B. Iversen, Exploration of phase compositions, crystal structures, and electrochemical properties of $Na_x Fe_y Mn_{1-y} O_2$ sodium ion battery materials, Chem. Mater. 30 (2018) 6636–6645, https://doi.org/10.1021/acs.chemmater.8b01566.
[50] X. Li, Y. Fan, B. Johannessen, X. Xu, K.W. See, W.K. Pang, O3-Type cathodes for sodium-ion batteries: recent advancements and future perspectives, Batter Supercaps 7 (2024) e202300618, https://doi.org/10.1002/batt.202300618.
[51] T. Risthaus, L. Chen, J. Wang, J. Li, D. Zhou, L. Zhang, D. Ning, X. Cao, X. Zhang, G. Schumacher, M. Winter, E. Paillard, J. Li, P3 $Na_{0.9}Ni_{0.5}Mn_{0.5}O_2$ cathode material for sodium ion batteries, Chem. Mater. 31 (2019) 5376–5383, https://doi.org/10.1021/acs.chemmater.8b03270.
[52] I. Hasa, D. Buchholz, S. Passerini, B. Scrosati, J. Hassoun, High performance $Na_{0.5}[Ni_{0.23}Fe_{0.13}Mn_{0.63}]O_2$ cathode for sodium-ion batteries, Adv. Energy Mater. 4 (2014) 1400083, https://doi.org/10.1002/aenm.201400083.
[53] X. Chen, X. Zhou, M. Hu, J. Liang, D. Wu, J. Wei, Z. Zhou, Stable layered P3/P2 $Na_{0.66}Co_{0.5}Mn_{0.5}O_2$ cathode materials for sodium-ion batteries, J Mater Chem A Mater 3 (2015) 20708–20714, https://doi.org/10.1039/c5ta05205j.
[54] H.M. Mudassir, C. Xie, F. Xia, R. Fang, Q. Chen, Z. Liu, T. Dong, F. Liu, S. Hu, Z. Jian, J. Wu, P2/P3 Biphasic layered oxide cathode enabled by additional electron-holes on oxygen for high-capacity sodium-ion batteries, J. Mater. Sci. Technol. 238 (2025) 230–237, https://doi.org/10.1016/j.jmst.2025.02.072.
[55] M.M. Rahman, J. Mao, W.H. Kan, C.-J. Sun, L. Li, Y. Zhang, M. Avdeev, X.-W. Du, F. Lin, An ordered P2/P3 composite layered oxide cathode with long cycle life in sodium-ion batteries, ACS Mater. Lett. 1 (2019) 573–581, https://doi.org/10.1021/acsmaterialslett.9b00347.
[56] X. Chen, J. Song, J. Li, H. Zhang, H. Tang, A P2/P3 composite-layered cathode material with low-voltage decay for sodium-ion batteries, J. Appl. Electrochem. 51 (2021) 619–627, https://doi.org/10.1007/s10800-020-01522-0.
[57] G. Derrien, J. Hassoun, S. Panero, B. Scrosati, Nanostructured Sn–C composite as an advanced anode material in high-performance lithium-ion batteries, Adv. Mater. 19 (2007) 2336–2340, https://doi.org/10.1002/adma.200700748.
[58] J. Hassoun, G. Derrien, S. Panero, B. Scrosati, A nanostructured Sn-C composite lithium battery electrode with unique stability and high electrochemical performance, Adv. Mater. 20 (2008) 3169–3175, https://doi.org/10.1002/adma.200702928.
[59] B. Boukamp, A package for impedance/admittance data analysis, Solid State Ionics 18–19 (1986) 136–140, https://doi.org/10.1016/0167-2738(86)90100-1.
[60] B. Boukamp, A nonlinear least squares Fit procedure for analysis of immittance data of electrochemical systems, Solid State Ionics 20 (1986) 31–44, https://doi.org/10.1016/0167-2738(86)90031-7.
[61] R. Dai, W. Sun, Y. Wang, Ultrasmall tin nanodots embedded in nitrogen-doped mesoporous carbon: Metal-Organic-Framework derivation and electrochemical application as highly stable anode for lithium ion batteries, Electrochim. Acta 217 (2016) 123–131, https://doi.org/10.1016/j.electacta.2016.08.051.
[62] Y. Liu, F. Fan, J. Wang, Y. Liu, H. Chen, K.L. Jungjohann, Y. Xu, Y. Zhu, D. Bigio, T. Zhu, C. Wang, In situ transmission electron microscopy study of electrochemical sodiation and potassiation of carbon nanofibers, Nano Lett. 14 (2014) 3445–3452, https://doi.org/10.1021/nl500970a.
[63] D.-J. Lee, J.-W. Park, I. Hasa, Y.-K. Sun, B. Scrosati, J. Hassoun, Alternative materials for sodium ion–sulphur batteries, J Mater Chem A Mater 1 (2013) 5256–5261, https://doi.org/10.1039/c3ta10241f.
[64] I. Hasa, J. Hassoun, S. Passerini, Nanostructured Na-ion and Li-ion anodes for battery application: a comparative overview, Nano Res. 10 (2017) 3942–3969, https://doi.org/10.1007/s12274-017-1513-7.
[65] J.M. Stratford, M. Mayo, P.K. Allan, O. Pecher, O.J. Borkiewicz, K.M. Wiaderek, K. W. Chapman, C.J. Pickard, A.J. Morris, C.P. Grey, Investigating sodium storage mechanisms in tin anodes: a combined pair distribution function analysis, density functional theory, and solid-state NMR approach, J. Am. Chem. Soc. 139 (2017) 7273–7286, https://doi.org/10.1021/jacs.7b01398.
[66] J. Ni, X. Zhu, Y. Yuan, Z. Wang, Y. Li, L. Ma, A. Dai, M. Li, T. Wu, R. Shahbazian-Yassar, J. Lu, L. Li, Rooting binder-free tin nanoarrays into copper substrate via tin-copper alloying for robust energy storage, Nat. Commun. 11 (2020) 1212, https://doi.org/10.1038/s41467-020-15045-x.
[67] M. Song, C. Wang, D. Du, F. Li, J. Chen, A high-energy-density sodium-ion full battery based on tin anode, Sci China Chem 62 (2019) 616–621, https://doi.org/10.1007/s11426-018-9422-y.
[68] R.F. Shahzad, S. Rasul, M. Mamlouk, I. Brewis, R.A. Shakoor, A.W. Zia, Designing tin and hard carbon Architecture for stable Sodium-Ion battery anode, Small Struct. 6 (2025) 2400367, https://doi.org/10.1002/sstr.202400367.
[69] Y. Xu, Y. Zhu, Y. Liu, C. Wang, Electrochemical performance of porous Carbon/Tin composite anodes for sodium-ion and lithium-ion batteries, Adv. Energy Mater. 3 (2013) 128–133, https://doi.org/10.1002/aenm.201200346.
[70] L. Minnetti, E. Barcaro, L. Sbrascini, F. Nobili, J. Hassoun, Chemical approach to achieve sodiated alloying anode for direct application in Na-ion battery, Mater. Res. Bull. 191 (2025) 113546, https://doi.org/10.1016/j.materresbull.2025.113546.
[71] D. Shanmukaraj, K. Kretschmer, T. Sahu, W. Bao, T. Rojo, G. Wang, M. Armand, Highly efficient, cost effective, and safe sodiation agent for high-performance Sodium-Ion batteries, ChemSusChem 11 (2018) 3286–3291, https://doi.org/10.1002/cssc.201801099.
[72] Y. Niu, Y. Guo, Y. Yin, S. Zhang, T. Wang, P. Wang, S. Xin, Y. Guo, High-Efficiency cathode sodium compensation for sodium-ion batteries, Adv. Mater. 32 (2020) 2001419, https://doi.org/10.1002/adma.202001419.
[73] J. Martinez De Ilarduya, L. Otaegui, J.M. López del Amo, M. Armand, G. Singh, NaN 3 addition, a strategy to overcome the problem of sodium deficiency in P2-$Na_{0.67}[Fe_{0.5}Mn_{0.5}]O_2$ cathode for sodium-ion battery, J. Power Sources 337 (2017) 197–203, https://doi.org/10.1016/j.jpowsour.2016.10.084.
[74] G. Singh, B. Acebedo, M.C. Cabanas, D. Shanmukaraj, M. Armand, T. Rojo, An approach to overcome first cycle irreversible capacity in P2-$Na_{2/3}[Fe_{1/2}Mn_{1/2}]O_2$, Electrochem. Commun. 37 (2013) 61–63, https://doi.org/10.1016/j.elecom.2013.10.008.
[75] A.J. Fernández-Ropero, M. Zarrabeitia, G. Baraldi, M. Echeverria, T. Rojo, M. Armand, D. Shanmukaraj, Improved sodiation additive and its nuances in the performance enhancement of sodium-ion batteries, ACS Appl. Mater. Interfaces 13 (2021) 11814–11821, https://doi.org/10.1021/acsami.0c20542.
[76] E. Barcaro, V. Marangon, D. Bresser, J. Hassoun, Scalable li-ion battery with Metal/Metal oxide sulfur cathode and lithiated silicon Oxide/Carbon anode, ChemSusChem 18 (2025) e202400615, https://doi.org/10.1002/cssc.202400615.
[77] X. Guo, S. Wang, J. Wang, H. Gao, Z. Huang, W. Lai, W.K. Pang, J. Qu, M. H. Nguyen, C. Yang, C. Dong, H. Liu, G. Henkelman, M. Armand, D. Aurbach, G. Wang, Unlocking the potential of phosphorus anodes for sodium-ion batteries via tailored reversible Na/Polyphosphide chemistry, Angew. Chem. Int. Ed. (2025) e202509929, https://doi.org/10.1002/anie.202509929.
[78] C. Kirst, E. Zonta, A. Kunz, A. Karger, M. Düsdieker, A. Frank, V. Savvin, B. Pham, J.P. Singer, A. Jossen, Plating onset detection and optimized charging profiles for lithium- and sodium-ion batteries, Electrochim. Acta 536 (2025) 146703, https://doi.org/10.1016/j.electacta.2025.146703.
[79] H. Hijazi, Z. Ye, L. Zhang, J. Deshmukh, M.B. Johnson, J.R. Dahn, M. Metzger, Impact of sodium metal plating on cycling performance of layered Oxide/Hard carbon sodium-ion pouch cells with different voltage cut-offs, J. Electrochem. Soc. 170 (2023) 070512, https://doi.org/10.1149/1945-7111/ace4fa.
[80] Y. Huang, L. Zhao, L. Li, M. Xie, F. Wu, R. Chen, Electrolytes and Electrolyte/Electrode interfaces in sodium-ion batteries: from scientific research to practical application, Adv. Mater. 31 (2019) 1808393, https://doi.org/10.1002/adma.201808393.
[81] J. Yang, J. Ruan, Q. Li, F. Fang, Y. Song, D. Sun, F. Wang, Improved low-temperature performance of Rocking-Chair Sodium-Ion hybrid capacitor by mitigating the de-solvation energy and interphase resistance, Adv. Funct. Mater. 32 (2022) 2200566, https://doi.org/10.1002/adfm.202200566.
[82] A.C.S. Jensen, H. Au, S. Gärtner, M. Titirici, A.J. Drew, Solvation of $NaPF_6$ in diglyme solution for battery electrolytes, Batter Supercaps 3 (2020) 1306–1310, https://doi.org/10.1002/batt.202000144.
[83] K. Westman, R. Dugas, P. Jankowski, W. Wieczorek, G. Gachot, M. Morcrette, E. Irisarri, A. Ponrouch, M.R. Palacín, J.-M. Tarascon, P. Johansson, Diglyme based electrolytes for sodium-ion batteries, ACS Appl. Energy Mater. 1 (2018) 2671–2680, https://doi.org/10.1021/acsaem.8b00360.
[84] I. Hasa, D. Buchholz, S. Passerini, J. Hassoun, A comparative Study of layered transition metal oxide cathodes for application in sodium-ion battery, ACS Appl. Mater. Interfaces 7 (2015) 5206–5212, https://doi.org/10.1021/am5080437.
[85] Y. Sun, G. Åvall, S.-H. Wu, G.A. Ferrero, A. Freytag, P.B. Groszewicz, H. Wang, K. A. Mazzio, M. Bianchini, V. Baran, S. Risse, P. Adelhelm, Solvent co-intercalation in layered cathode active materials for sodium-ion batteries, Nat. Mater. 24 (2025) 1441–1449, https://doi.org/10.1038/s41563-025-02287-7.
[86] W. Zuo, A. Innocenti, M. Zarrabeitia, D. Bresser, Y. Yang, S. Passerini, Layered oxide cathodes for sodium-ion batteries: storage mechanism, electrochemistry, and techno-economics, Acc. Chem. Res. 56 (2023) 284–296, https://doi.org/10.1021/acs.accounts.2c00690.
[87] L. Merker, M. Blessing, B. Zhang, H.S. Stein, Information dense and industry scalable accelerated Formation, Advanced Intelligent Discovery (2025) 202500025, https://doi.org/10.1002/aidi.202500025.
[88] A. Kempf, P. Adelhelm, M. Graczyk-Zajac, An electrochemical Study on the impact of charging parameters on the electrochemical performance of alloy-based C/Sn composite anodes for sodium-ion batteries, Batter Supercaps 8 (2025) e2500340, https://doi.org/10.1002/batt.202500340.